Abstract

Title of Thesis:	*IN SITU* INFRARED DIAGNOSTICS FOR A MICRO-SCALE COMBUSTION REACTOR
Degree Candidate:	Scott Heatwole
Degree and year:	Master of Science, 2004
Thesis directed by:	Assistant Professor Steven G. Buckley
	Department of Mechanical Engineering

The development of centimeter to millimeter scale engines and power supplies have created a need for micro-scale combustion diagnostics. Fuel concentrations, product concentrations, and temperature are useful measurements in determining combustion behavior, chemical efficiency, and flame structures. However, to the present there have been few efforts to develop non-intrusive diagnostic techniques appropriate for application in such small engines. Non-intrusive measurements in these engines are complicated by short path length and lack of optical access. In this thesis *in situ* FTIR spectroscopy is used to measure temperature and concentrations of fuel, and carbon dioxide in a micro-combustor. The measurements are made through silicon walls spaced a few millimeters apart. This is possible because silicon is transmissive in the

infrared. Experimental issues, including the optical setup, limitations associated with etaloning, calibration, and interpretation of the resulting spectra using wide-band models are discussed in detail.

IN SITU INFRARED DIAGNOSITICS FOR A MICRO-

SCALE COMBUSTION REACTOR

by

Scott Heatwole

Thesis submitted to the Faculty of the Graduate School of the
University of Maryland, College Park in partial fulfillment
of the requirements for the degree of
Master of Science
2004

Advisory Committee
Assistant Professor Steven G. Buckley, Chair/Co-advisor
Assistant Professor Christopher Cadou, Co-advisor
Associate Professor Gregory Jackson

Dedication

To my parents (Proverbs 22:6)

and

To Kristine

Acknowledgements

There have been a number of people who have been helpful in the completion of my graduate work and I would like to formally thank these people and express my gratitude for the assistance they have offered.

I am grateful to my advisor, Steven Buckley for his direction during my research. He helped steer me in the right direction and ensured that all necessary details had been taken care of. I would like to thank Chris Cadou for his assistance in supporting my research and editing this document. I would like to thank the members of my committee professors Steve Buckley, Chris Cadou and Gregory Jackson for their assistance in completing all the necessary requirements. I would like to thank Anand Veeraragavan, whose was of immense help in completing this project. Also, I would like to thank Tim Leach who provided much advice and insight.

Table of Contents

List of Figures

List of Tables

Chapter 1 - Introduction

1.1 – Motivation

Silicon MEMS technology has enabled the miniaturization of a wide range of devices. All of these require power and so there is a similar trend to create small, high energy density source of power. The potential applications for a micro-power source include miniature rockets for micro satellites, power for micro unmanned aerial vehicles, and small electrical power sources to replace batteries. Many of these devices would have length scales less 1 mm.

Before attempting to develop new micro-scale power supplies, it is natural to investigate currently available technologies. The only currently available commercial technology for energy storage in volumes less than 100 mm^3 is electrochemical batteries. However combustion based systems have a huge advantage with respect to batteries when compared on an energy basis. For example, the specific energy of the best batteries currently produced is approximately 150 watt-hr/kg for the Li-Ion battery [1]. The specific energy of a hydrocarbon fuel such as methane is on the order of 10,000 watt-hr/kg; two orders of magnitude greater than batteries. On this basis, therefore, even with losses associated with extracting power from the fuel, a micro-combustion based heat-engine may be an excellent alternative to batteries. For example, a heat engine that could convert chemical energy to power at an efficiency of 10% (considered bad by the standards of macro-scale engines) would still produce an order of magnitude more power than the best battery. A micro-scale device that could harness the chemical energy of the fuel would thus enable significant increases in the power output or endurance of in micro-

scale power sources. An additional advantage is the fact that the shelf life of chemical fuels is in most cases very long, while batteries have a more limited shelf life.

The surface to volume ratio of a combustor increases as the combustor gets smaller and this leads to several limitations not typically encountered in conventional combustors. First, since heat transfer away from a flame is proportional to surface area while heat generation is proportional to the volume, decreasing the size of a combustor can eventually quench the flame. Second, conduction through the combustor structure can pre-heat the reactants leading to a broadening of the reaction zone before quenching occurs [2]. Third, chemical activity is also affected by the surface to volume ratio. As surface to volume increases, there is an increased number of collisions with the wall and hence an increase in the number of active radical species that are destroyed. Since these radicals are essential in the breakdown of fuel, forming of products and release of heat [3], the chemical affinity of surface itself can also play an important role in quenching a flame. Fourth, flows in small tubes and channels have comparatively low Reynolds numbers, which means that hydrodynamic losses can be proportionally greater compared to macro-scale flows. The reason is that small length scales result in large velocity gradients, which lead to large frictional losses [4]. The low Reynolds number also means mixing will be limited by molecular diffusion [5]. The slower rate of diffusion hinders mixing of the oxidizer and fuel so in non-premixed systems longer residence times are needed.

1.2 – Relevant Previous Work

1.2.1 – Micro-combustion

There is extensive classical literature on the importance of heat loss and chemical quenching on flame propagation and extinction that is directly applicable to the micro-scale combustion problem [6-8]. Micro-scale studies have provided a fresh look into combustion quenching and extinction phenomena. Daou and Matalon have studied the interaction between the effects of velocity, heat loss to the structure, and passage width on premixed flames in channels with constant temperature walls [9]. In a 1-D model of a heat recirculating burner, Ronney has shown that heat conduction within the structure is the dominating effect in heat recirculating burners [10]. Work by Leach et al. has also shown that axial conduction of heat through the wall plays a major role in determining micro-combustor performance [2, 11]. Using a simple 1-D model of a flame held between two infinitely long plates, Leach showed that axial conduction and conjugate heat transfer causes the reaction zone to broaden and the burning rate to increase. Work by Raimondeau et al. has shown that quenching of radicals at the wall is also a key player in flame propagation in micro-channels [12].

1.2.2 – Micro-power Sources

There are several research efforts in progress to produce a micro-engine. The different types of micro-combustors/engines being developed include micro-rotary engines, micro-turbines, micro-HCCI engines, micro-free-piston engines and micro-heat recirculating combustors. These are detailed below.

Fernandez-Pello and co-workers are developing a micro-rotary engine that is expected to produce ~10-100 mW of power with a 1 mm rotor [13]. The mini-rotary engine is EDM-fabricated from with a displacement of 0.064 mm^3. Using a rotary design without valves helps simplify the design of the micro-device, as sealing and actuation of micro-valves requires substantial complexity.

MIT is developing a MEMs micro-turbine [14]. The aim is to produce 10-50W of power from a turbine the size of 2.1cm x 2.1cm x 0.38cm. The design uses six individual layers of silicon, with the turbine, combustor and housing all being made of silicon. In the current device, there are issues with completion of the chemical reaction. For the desired power and mass flow the combustion time is too long compared to the residence time and unreacted fuel exits the combustor and reactions continue into the turbine. Hence one of the primary remaining challenges for this device is combustion-related.

Kittelson's group is pursuing a homogenous charge compression ignition (HCCI) micro-engine capable of producing 10W [15, 16]. An HCCI engine compresses a mixture of fuel and air until it ignites spontaneously. This has several advantages over typical compression ignition engines, including reducing NO_X by enabling the mixture to burn extremely lean mixtures, eliminating limitations on compression ratio, eliminating external ignition systems, and enabling a wide variety of fuels to be used. One advantage of HCCI on the micro-scale is the lack of external ignition. This makes the design less complex and avoids the problem of achieving appropriate ignition energies at diameters below the quenching diameter of the mixture. The free piston design of the proposed system can compress a gas used

to deliver mechanical power or can be coupled with a permanent magnet generator. In a similar vein, Menon and co-workers have been developing a spark ignition reciprocating free piston engine [17]. This engine will be coupled in some way to a generator to produce electric power.

Ronney et al. have done work on heat recirculating burners for use with thermoelectric generators [10, 18, 19]. The burners are a 'Swiss roll' design and work by allowing heat to be exchanged between product and reactant streams. The counter-current heat exchanger design greatly reduces heat loss to the environment. The total reactant enthalpy (sum of thermal and chemical enthalpy) is higher for the preheated reactants than for a cold incoming stream and thus preheated reactants can sustain combustion under conditions in which a flame without recirculation would be extinguished. By coupling this burner with a thermoelectric generator, electric power could be produced. The advantage of this design is that no moving parts are required. Yetter and colleagues have also done work on heat recirculating burners, using a micro-fabricated burner, with 800 μm channels and a 0.1 m total path [20]. Using catalytic walls and a hydrogen/air flame, surface temperatures as high as 600 K were reached in the combustor.

Work on igniters for micro-combustors has been done by Zhang et al. [21]. Thin-film polysilicon igniters are deposited onto the silicon of the micro-engine. An electric current is passed across the thin film, causing resistive heating which in turn initiates combustion. Temperatures as high as 900°C have been achieved on the surface of these igniters which are intended for use in micro-gas turbines.

Micro-rockets for micro-satellite positioning are also under development. Micro-rockets with a impulse of 10^{-4} N/s and 100W of power have been developed by Fernandez-Pello and co-workers [13]. Also, Epstein et al. are developing a high-pressure, bipropellant micro-rocket with a chamber pressure of 12 atmospheres with a projected thrust of ~25 N [22].

1.2.3 - Micro-diagnostics

As mentioned previously, the combination of small volumes with the presence of high temperatures and oxidizing reactions has prevented the use of most combustion measurement tools for determining performance used on the macro-scale. However, diagnostics for measuring temperature and velocity have been developed with some success. Work by Zhang and co-workers on igniters has also been used to develop micro-fabricated thermocouples [21]. The micro-thermocouples are made by depositing polysilicon conductors onto a silicon wafer combustor. The resistance of the polysilicon conductor is measured as it changes with changes with temperature so measuring resistance gives the temperature. These thermocouples are effective for low temperature reacting flows found in catalytic systems, but they are unable to survive stoichiometric combustion temperatures. Breuer has taken advantage of silicon's transmissivity in the infrared to measure velocity using micro-Particle Imaging Velocimetry (PIV) [23].

1.2.4 – *In Situ* Infrared Diagnostics

There is a large body of literature on in in-situ FTIR spectroscopy for measuring temperature and concentration in combustors [24-26]. In combustion

6

measurements using FTIR spectroscopy, there are two methods for acquiring the spectrum of a sample: transmission and emission spectroscopy. In transmission FTIR spectroscopy, a beam is sent through the sample and the light that is absorbed by the molecules is measured by a detector positioned to collect the beam as exits the sample. In emission FTIR spectroscopy, emitted radiation from the sample is collected by an optical system, is passed through the spectrometer which serves as a tunable filter, and is collected and measured by a detector.

Emission FTIR is commonly used in combustion measurements since the high temperatures of the combustion environment cause thermal excitation of vibrational transitions of most molecules yielding a large amount of radiative energy that makes detection relatively easy. Emission experiments have the advantage that there is no beam to send through the sample to be collected by a detector. This makes the setup much less complicated, reducing the number of optical components and concerns about thermal beam steering. Also, this allows remote sensing measurements of radiative sources at a distance. For example, Hilton et al. used emission FTIR to make remote measurements of smokestack exhausts [26]. Measurements of CH_4, CO, CO_2, and H_2O were made, and the HITRAN database was used to calculate temperatures, since the exhaust was less than 100°C. Heland et al. used emission spectroscopy to measure the temperature of CO_2 in hot combustion exhaust gases [25]. The HITEMP database was used to infer gas temperatures based on the CO_2 spectra. Jaquot et al. measured temperatures of hot combustion exhaust gases using emission spectroscopy [24]. They used the EM2C narrow band model to infer gas temperature from CO_2 spectra. Measurements of

temperatures up to 1100 K have also been made. Bailly et al. used a high resolution spectrometer (0.02 cm^{-1}) to infer gas temperature from CO_2 spectra by only considering the transitions that are excited at high temperatures [27]. The temperatures were obtained with precisions on the order of ±1% for this method.

Transmission FTIR is the most common form of FTIR spectroscopy because the sample does not have to be at the high temperatures needed for emission measurements. In this technique, a beam is sent through the sample and the molecules absorb light. One particularly relevant investigation to the work presented here is that of Lindner and co-workers who used FTIR measurements to infer gas temperature, CO_2 concentration and combustion efficiency [28]. They used an in-house wide band model with constants obtained from the literature to compute gas temperature and concentrations. Both emission and absorbance measurements were used in this experiment. Koshland et al. used in situ transmission FTIR to detect chlorinated hydrocarbons in a combustion flows [29]. Modest et al. has done work on comparing Hitran, Hitemp, Radcal, and EM2C using an isothermal drop-tube burner and transmission spectroscopy [30]. Their results indicated that the wide band models are better able to predict the band structure at higher temperatures (i.e. > 1300K) with EM2C being slightly better than Radcal in this respect.

1.3 – Purpose and approach

The purpose of this work is to develop a diagnostic tool for use in measuring temperature and species concentration (primarily methane, carbon dioxide, and carbon monoxide) in silicon walled micro-combustors using FTIR spectroscopy. The spatial resolution is intended to be better than 1 mm and the measurements are

intended to take advantage of the fact that silicon is transparent in the infrared by making the measurements directly through the silicon walls.

The technique will be demonstrated in a simple silicon walled combustor constructed using conventional (non-MEMS) manufacturing techniques. A model of carbon dioxide absorption will be developed and used to infer gas temperature measurements from the infrared spectra. Calibrating the absorption signal using various gas mixtures will enable the determination of species concentration from absorption spectra.

Chapter 2 – Experimental Apparatus

2.1 – Experimental Setup

To simulate a silicon-based micro-combustor, a flame is stabilized between two silicon wafers spaced a few millimeters apart. Figure 2-1 shows a schematic diagram of the experiment. Two UFC-3000A mass flow controllers (MFCs) from Unit Instruments meter the flow of the reactants (methane and air) into a mixing chamber which consists of a 1-1/4" diameter steel pipe filled with steel wool. This ensures that the gases are well-mixed before they flow into the combustor. A 15 μm Milipore filter placed after the mixing chamber acts as a safety measure to prevent flashback. The final part of the flow system is the burner itself which rests on a lab jack in order to translate the burner vertically in the beam path.

With the lab jack lowered to its minimum height, the interrogation region is 54 mm downstream from the inlet. When the lab jack is raised until the bottom of the mask touches the top of the sliding plate on the burner, the interrogation region is 14 mm downstream from the inlet. Thus for flame measurements in the micro-combustor, flames positioned between 14 mm and 54 mm downstream from the inlet can be interrogated and the maximum streamwise traverse is 40 mm.
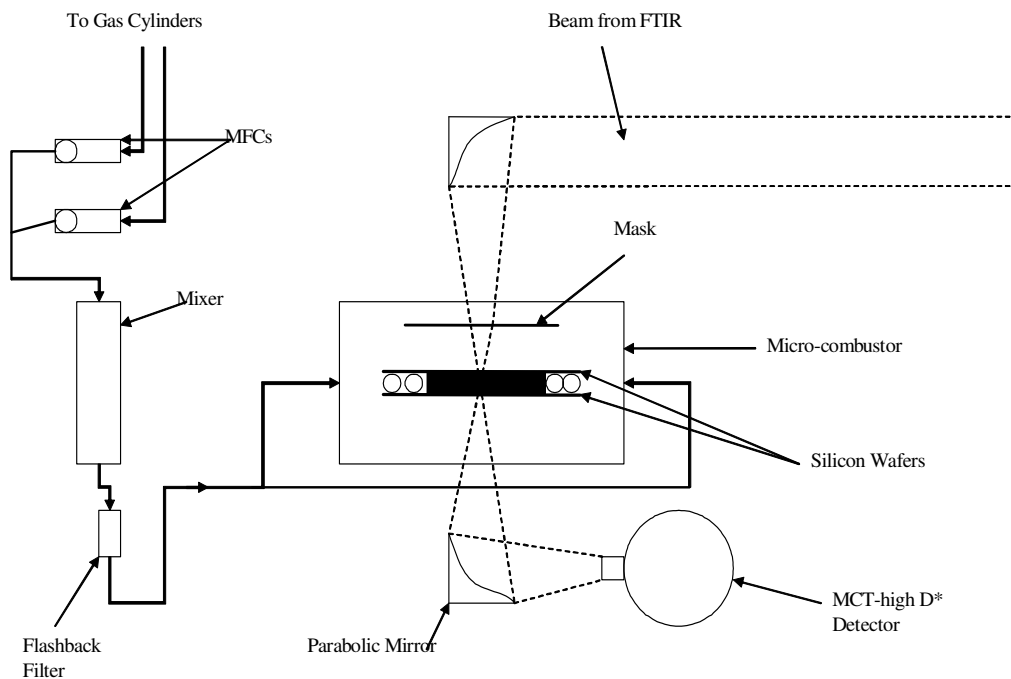
Figure 2-1: Schematic of experiment

A Thermo-Nicolet Nexus 870 FTIR spectrometer is used to collect the absorption spectra. To achieve the desired spatial resolution (1 mm or less), an external optical system is used to reduce the diameter of the FTIR beam and pass it through the combustor. The combustor is located on an optical table adjacent to the FTIR. Figure 2-2, shows the pair of 90-degree parabolic mirrors used to direct the interrogation beam outside the FTIR, through the burner, and onto the FTIR's MCTA* (Mecury Cadium Telluride) detector which is removed from the instrument bench and attached to the optical table.
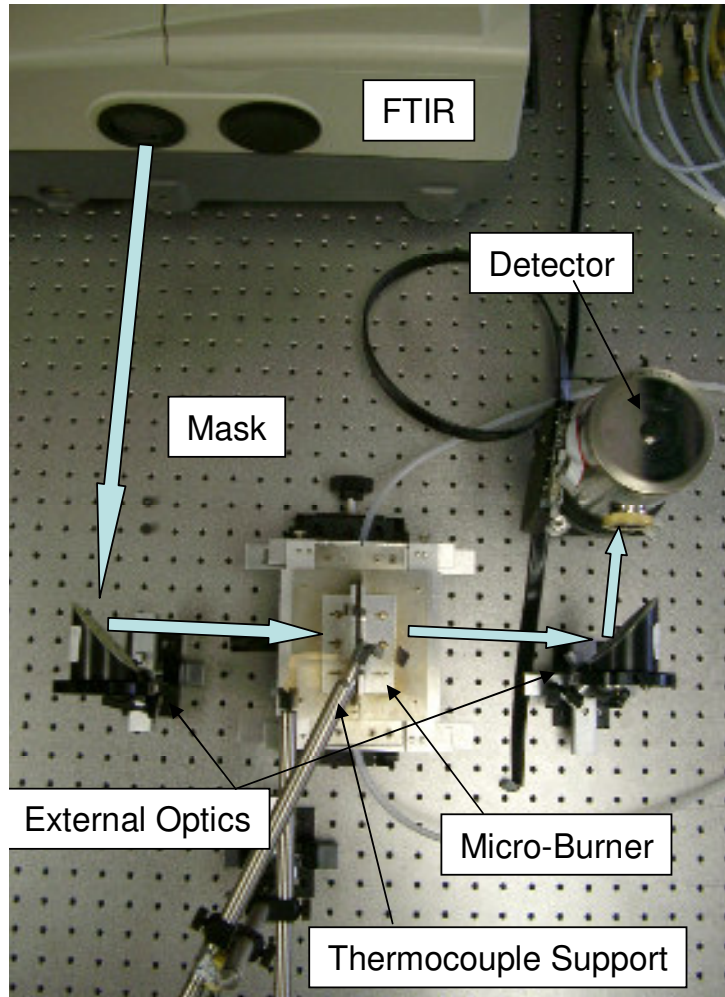
Figure 2-2: Top view of optical setup

The first parabolic mirror (M1) has a focal length of 190 mm and reduces the beam diameter from approximately 38 mm to 10 mm. The second parabolic mirror (M2) has a focal length of 50.8 mm and directs the transmitted beam onto the detector. The burner is placed at M1's focal point and a horizontal slit cut in a piece of brass shim stock is placed immediately in front of the combustor. This serves as a mask to reduce the size of the interrogated region and hence the spatial resolution of the measurement to 1 mm in the flow direction. Figure 2-3 shows a side view of the setup with the burner supported by a vertically adjustable jack. Raising or lowering

the jack traverses the interrogation volume in the flow direction, making it possible to collect spectra (and thereby measure species concentration and temperature) as a function of streamwise position in the flame. Lastly, an Omega 0.01" diameter k-type ungrounded thermocouple with a stainless steel sheath is used to interrogate the gas temperature in the combustor and as a check on the spectroscopic measurements. The tip of the thermocouple is positioned in the middle of the interrogation beam from the FTIR.
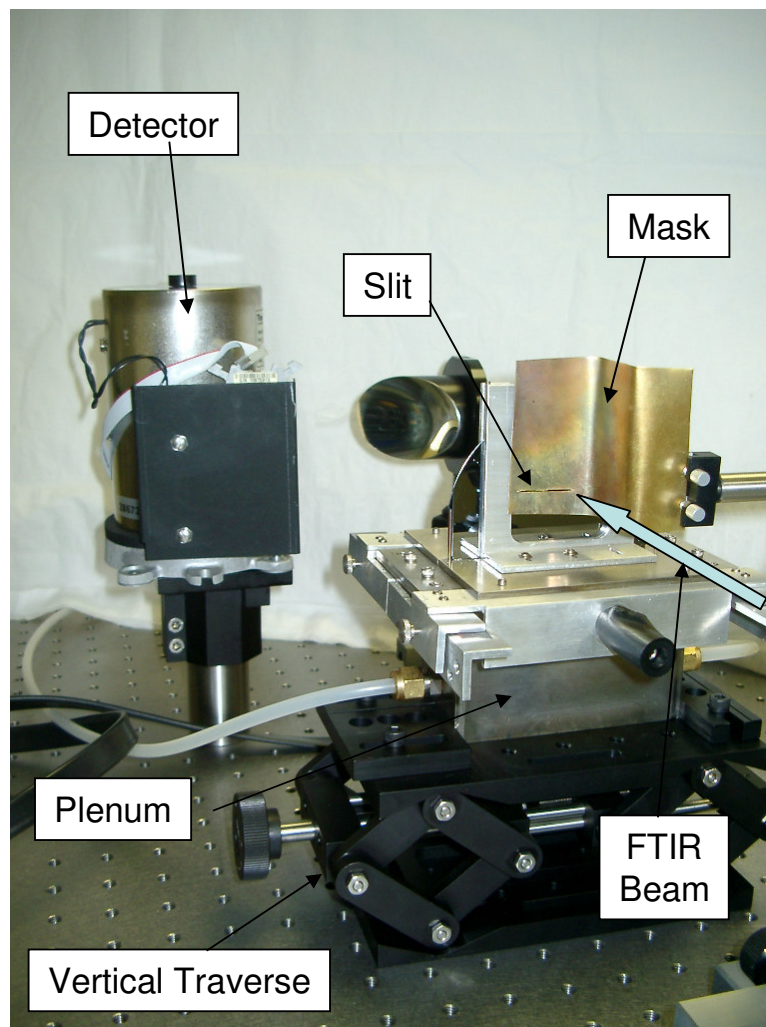
Figure 2-3: Side view of optical system

2.2 - Burner Design

For this experiment, a small-scale burner was devised which would simulate the behavior of a silicon based MEMs micro-combustor while avoiding the costs associated with MEMs fabrication. The burner consists of two silicon plates (wafers) that are held parallel to each other but can be adjusted to vary the plate spacing. Figure 2-4 is a drawing of the micro-burner showing the various critical components.

Pre-mixed fuel and air are introduced into the combustor plenum and pass vertically upward between the two silicon plates. Two vertical guides support the wafers on the outside and a set of 4 vertically-oriented stainless-steel tubes (two at each wafer edge) support the wafers from the inside. The diameter of the tubes fixes the minimum wafer spacing. This can be seen more clearly in Figure 2-5 which is a top view. The two wafers are held on different plates to allow for adjustment of the plate spacing. P-type and n-type silicon wafers 500 microns thickness with a 100 orientation were used.

When the burner was initially tested, it was noticed that there was entrainment of air along the sides of the burner. To eliminate this, several c-shaped pieces of aluminum flashing, roughly 8 cm tall and 2 cm wide were constructed to fit around the ends of the silicon wafers. These pieces were then filled with glass insulation in order to prevent air entrainment of room air into the burner

14
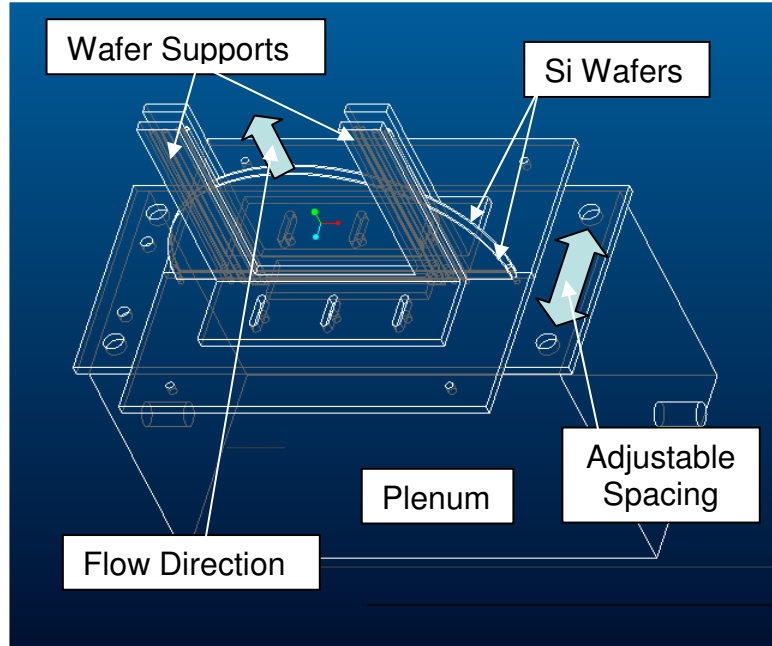
Figure 2-4: 3-D view of burner assembly
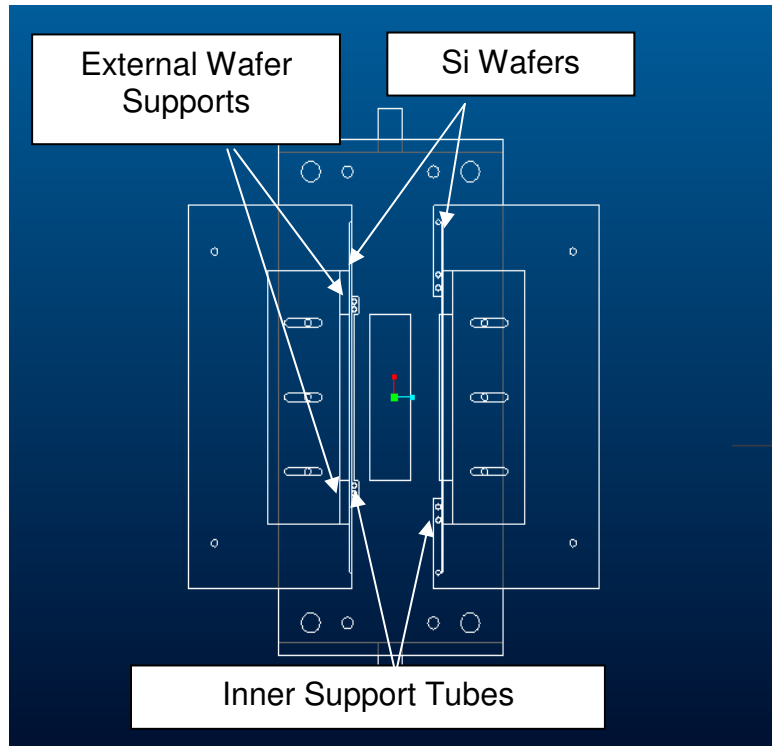
Figure 2-5: Top view of burner.

2.3 – Experimental Procedure

First, an ambient background scan is acquired with the burner cold and the gas flows off before collection of flame data. Next, the equivalence ratio is set, the burner is lit and the system is allowed to run for a period of time to allow it to come to a thermal steady state with the surroundings. This requires approximately 15 minutes. 100 individual spectra are acquired after the burner has come to equilibrium. These are subsequently averaged to reduce the noise. Dividing the sample spectrum by the background spectrum yields a properly normalized transmittance from which species concentration and temperature can be computed. Each spectrum is taken at 16 cm^{-1} resolution to reduce the acquisition time to 20 seconds per 100 scans. The largest possible aperture setting is used to maximize beam intensity. To make measurements at higher spectral and spatial resolutions, the aperture size will need to be reduced.

2.4 – Silicon Wafers

The transmission of light by the silicon wafers enables the in situ FTIR measurements in this project. However, the level of doping in the silicon wafer has a strong influence on silicon's absorption coefficient which rises with higher doping levels for both P and N type dopants [31, 32]. Two types of wafers were used in this experiment: a p-type doped with Boron with both sides polished, and an n-type doped with Phosphorus with only a single side polished. Both wafer types were described as 'lightly' doped by the manufacturer but the specific level of doping is unknown. The wafer resistivity was 10-100 Ohm-cm for both types of wafers. Since

wafer resistivity falls with doping and the resistivities of the wafer are relatively high, it appears reasonable that the doping level is low.

The transmittance of several lightly doped silicon wafers each having different surface roughnesses is shown in Figure 2-6. Transmittance was measured directly in the burner described previously by comparing a background scan with no plates in the path to one made with a single plate in the optical path. The data show that at room temperature, silicon wafers with both sides polished are roughly 60% tranmissive in the range 3300 to 2000 cm^{-1}. This is the region where the methane and carbon dioxide vibrational bands of interest here are located. The lower values for the single side polished and unpolished wafers are due to the roughness of the unpolished surfaces. These act like diffusers and scatter the light from the interrogation beam out of the optical path. The single side polished wafer has less scattering than the completely unpolished wafer because there is only one diffusing surface.

17
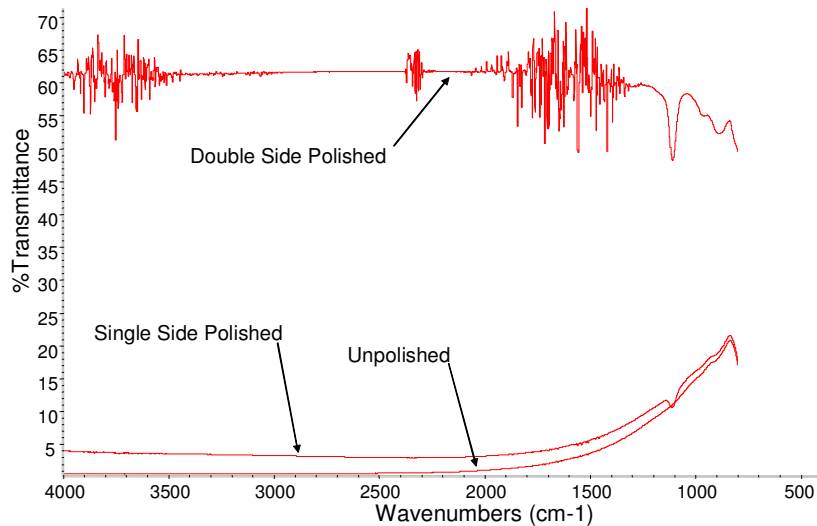
Figure 2-6: %Transmittance of both sides polished, single side polished, and unpolished 500 μm thick wafers

Figure 2-7 compares the transmittance of the silicon wafers to the absorption features of CO_2 and CH_4 that we seek to measure. The figure shows that the transmittance is approximately constant (~60%) across the CH_4 band but changes significantly over about half of the CO_2 band. This presents a challenge for the CO_2 -based temperature measurements that will be discussed later in more detail.
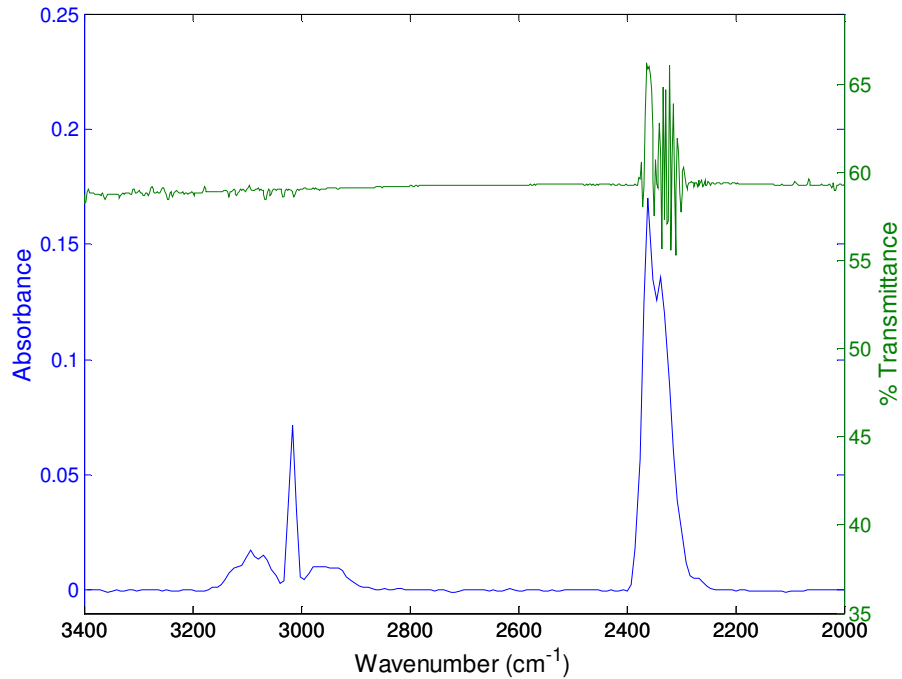
Figure 2-7: Absorbance spectra of CO_2 and CH_4 in the burner and transmittance of the double side polished silicon wafer

18

Chapter 3 – Absorption Spectroscopy

Energy is stored in molecules in discrete rotational, vibrational, electronic, and nuclear modes. As a result, when a photon (light) strikes a molecule, it can only be absorbed if the energy of the photon corresponds to the difference in energy between two of these discrete levels. Quantum mechanical selection rules determine which transitions are allowed. The net result is that molecules have complex absorption spectra with features that correspond to the various electronic, vibrational, and rotational transitions that are allowed for the particular molecule under consideration. The absorption measurements reported here for CO_2 and CH_4 involve relatively low energy photons in the infrared region of the spectrum and hence only rotational and vibrational features will be probed.

Since CO_2 is a linear molecule, there are four vibrational modes: two corresponding to bending, one corresponding to symmetric stretching, and one corresponding to asymmetric stretching. The feature considered here is the asymmetric stretch mode centered at approximately 2350 cm^{-1}. The absorption of CH_4 is more complex because the molecule is tetrahedral; the absorption features we consider here are in the 3000 cm^{-1} region.

The Beer-Lambert law describes the relationship between the absorbed signal and the concentration of the absorbing species:

$$\frac{dI(\bar{V})}{I_0(\bar{V})} = -k(\bar{V}) \cdot C \cdot dx \tag{1}$$

In this expression, I_0 is the initial light intensity, dI is the measured change in transmitted intensity due to the absorbing sample, $\bar{V}$ is optical frequency (typically in

cm^{-1} for infrared measurements) , C is the concentration, dx is the differential path length, and k is an absorption coefficient that depends on the optical frequency (or wavelength). Integrating over the optical path length gives:

$$\ln \frac{I_0(\bar{V})}{I(\bar{V})} = k(\bar{V})CL \tag{2}$$

where L is the pathlength. Converting natural logarithms to base 10 gives:

$$\log_{10} \frac{I_0(\bar{V})}{I(\bar{V})} = A(\bar{V}) = \varepsilon(\bar{V})CL \tag{3}$$

where A is the absorbance and ε is the molar absorptivity which is a function of optical frequency. The fact that the absorbance is proportional to pathlength presents a challenge at the micro-scale when path lengths are very short. However the species of interest here (CO, CO_2, H_2O, and CH_4) are present in relatively large concentrations so we can trade species sensitivity for path length and achieve measurable absorbance over relatively short path lengths of 1-2 mm. The concentration of the sample is computed using

$$C = \frac{\bar{A}}{\bar{\varepsilon}L} \tag{4}$$

where $\bar{A}$ is the wavelength integrated absorbance and $\bar{\varepsilon}$ is the average absorption coefficient.

The value of the wavelength-integrated absorbance was calculated by summing the absorbance over all lines in the ro-vibrational band:

$$\bar{A} = \int \log_{10} \frac{I_0(V)}{I(V)} dV \tag{5}$$

Similarly, the average absorption coefficient is:

$$\bar{\varepsilon} = \int \varepsilon(\nu)d\nu \qquad\qquad (6)$$

The error introduced by assuming that $\bar{\varepsilon}$ remains constant with changes in temperature is small since $\bar{\varepsilon}$ is a relatively weak function of temperature and the vibrational populations of the molecules being studied are relatively weakly perturbed (ie. by no more than 15% of their room temperature values).

3.1 – FTIR Spectroscopy

A Fourier Transform Infrared spectrometer consists of a broadband infrared source, a Michelson interferometer and a detector. The Michelson interferometer acts like a tunable optical filter and consists of two mirrors and a beam splitter as shown in Figure 3-1. The light from the source is split by the beam splitter and bounces off each mirror and recombines. By varying the position of the active mirror, it is possible to change the path lengths of the two beams causing them to interfere over a range of wavelengths. In most FTIR spectrometers, the active mirror moves (is scanned) and the detector measures intensity reading as a function of time. This is known as an "Interferogram". The rate of passage of interference fringes from a Helium Neon (HeNe) laser reference beam that also follows the same optical path enables determination of the scan rate. A Fourier transform of this time-varying signal at the detector enables one to determine intensity function of wavelength.
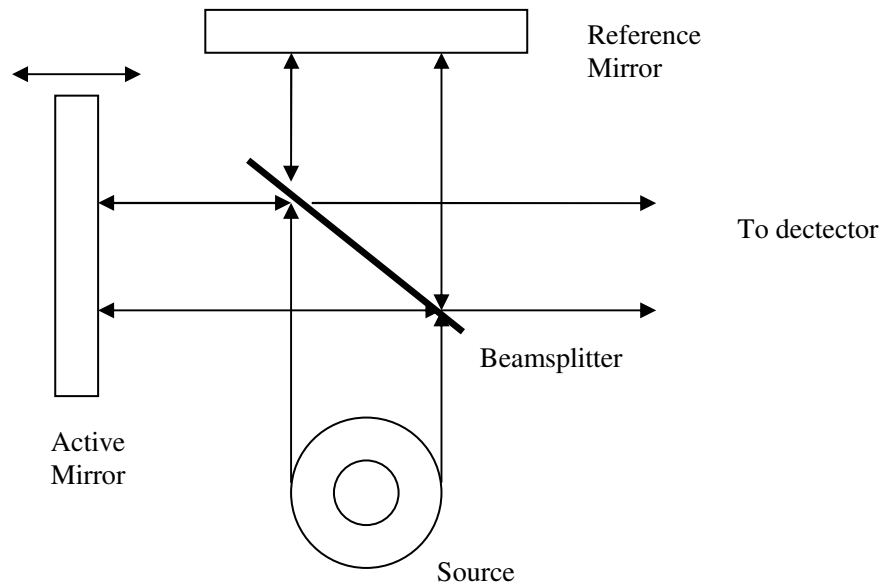
Figure 3-1: Schematic of a Michelson Interferometer

3.2 – Method for Computing Species Concentration

After collecting the sample absorbance spectrum, the raw spectrum is imported into Matlab for correction and analysis. First, the baseline absorbance is found by fitting a 2nd order polynomial to the portions on either side of the band where there is no absorption from gas-phase species. Next, the baseline is subtracted from $A(v)$ to correct for losses in the optical path that are not related to absorption from the species of interest. Figure 3-2 shows an uncorrected CO_2 spectrum and Figure 3-3 shows a CO_2 spectrum whose baseline has been corrected. Once the baseline of the sample spectra is corrected, the CO_2 concentration and gas temperature can be calculated.

As will be discussed later, the transmittance of the silicon wafers changes with temperature. This creates a potential problem because the reference spectrum

associated with I_0 is recorded at low (room) temperature. We can determine how this affects the data interpretation by defining a function $x(\bar{v})$ that, when multiplied by $I_0(v)$ at room temperature, gives $I_0(v)$ corresponding to combustion temperatures. Incorporating this into Equation 3 gives:

$$A(\bar{v}) = \log_{10} \frac{x(\bar{v}) I_0(\bar{v})}{I(\bar{v})} = \log_{10} \frac{I_0(\bar{v})}{I(\bar{v})} + \log_{10} x(\bar{v}) \tag{7}$$

Equation 7 shows that the temperature variation of the silicon absorption spectrum manifests itself as a baseline shift. Therefore, the baseline subtraction correction also accounts for the temperature variation of the silicon wafer's absorbance.
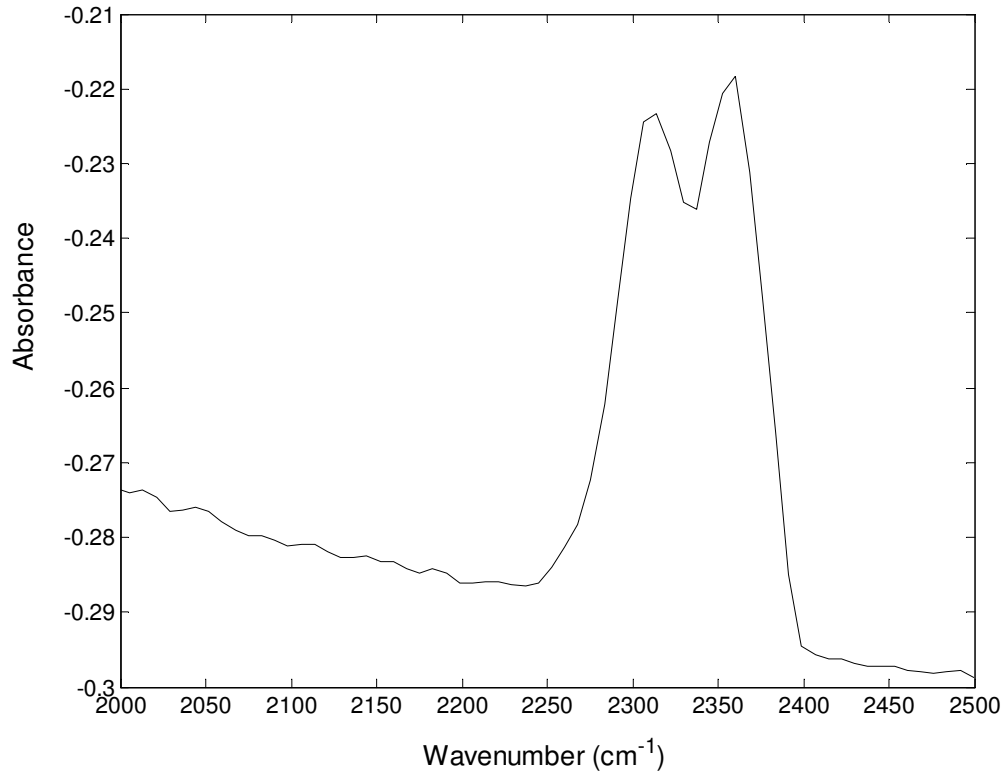
Figure 3-2: CO$_2$ spectra with uncorrected baseline: ϕ = 0.86, U = 44 cm/s, 2.15 mm wafer spacing
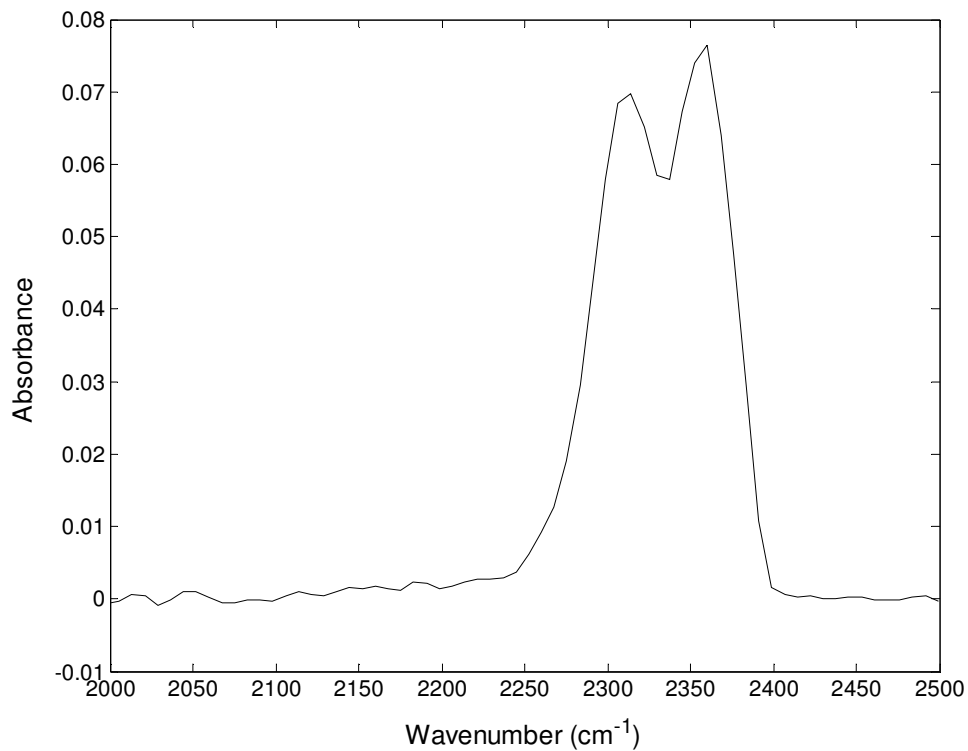
Figure 3-3: CO_2 spectra with corrected baseline: ϕ = 0.86, U = 44 cm/s, 2.15 mm wafer spacing

3.2.1 – Calibration of CO_2 Concentration

The technique was calibrated by using mass flow controllers (MFCs) to create known CO_2-air mixtures in the burner. Spectra were acquired and $\overline{A}$ was computed using Equation 5 for each mixture enabling the product $\overline{\varepsilon}L$ to be determined from a plot of $\overline{A}$ versus concentration. This avoids errors associated with measuring the path length, which can become quite significant on small scales, and avoids difficulties with determining $\overline{\varepsilon}$.

Figure 3-4 is a calibration plot showing how integrated absorbance varies with concentration. Note that the relationship is linear and that it is therefore

consistent with Beer's Law. The calculation of the error bars are reviewed in Appendix C. The line describing the least squares linear fit is:

$$C_{CO_2} = 4.02e-4 \cdot \overline{A}_{band} - 5.07e-5 \qquad (8)$$

The fact that the x intercept in Equation 8 is small is reassuring; it should be close to zero, within the estimated uncertainty of the measurements. The concentration of CO_2 in an unknown sample spectrum can now be determined using Equation 8 and measurements of the area under the CO_2 absorption band $\overline{A}_{band}$.
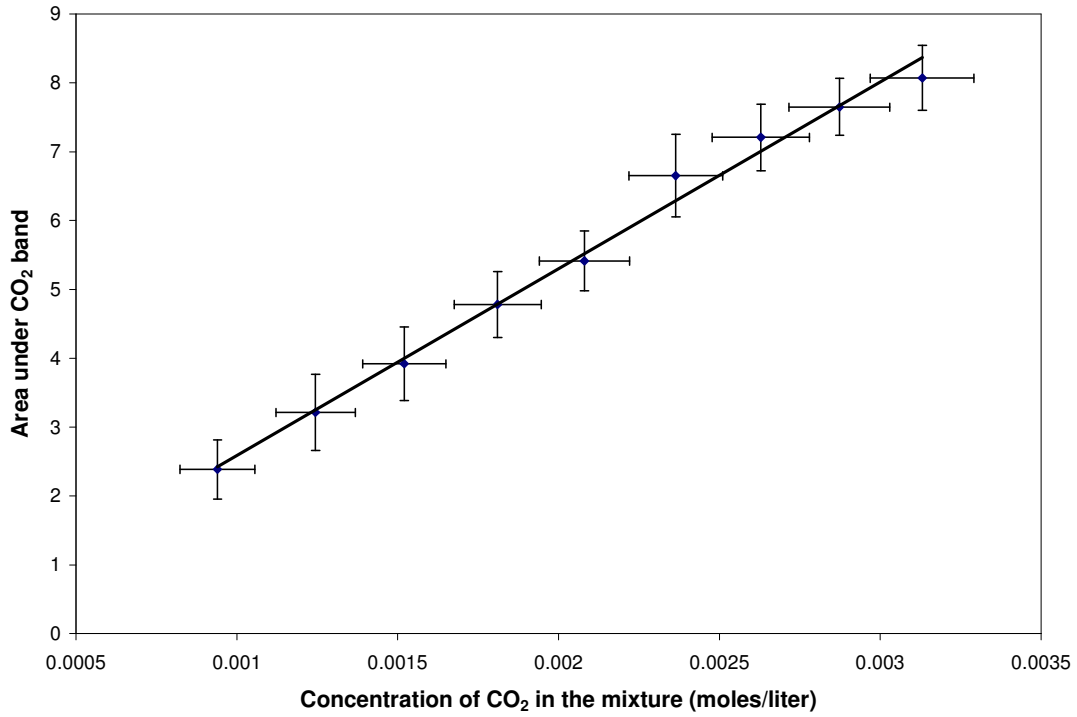
Figure 3-4: CO$_2$ calibration line for 2.15 mm wafer spacing

3.2.2 - CH$_4$ Concentration

A different approach was used to find the concentration of CH$_4$ due to the fact that CH$_4$ has a smaller area under the P and R branches for a given concentration

and that the Q branch is very large, as shown in Figure 3-5. As a result, instead of calculating the area, the absorbance of the peak of the Q branch was used to generate the calibration line. This reduces the level of variability in the data by excluding the P and R branches that are much weaker, and therefore have a much smaller signal to noise ratio (and error) than the measurement of the peak of the Q branch. Also, since the Q branch peak has a much higher absorbance than the P and R branches, the detection limit for CH_4 is lowered.
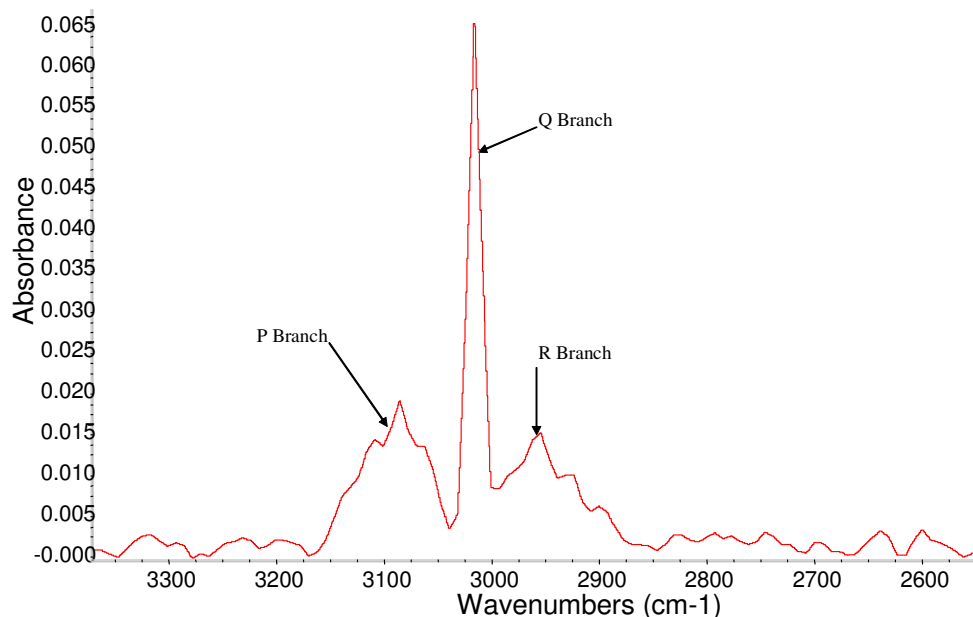
Figure 3-5: Typical CH$_4$ spectra

Figure 3-6 shows the calibration data and the least squares linear fit for concentration as a function of the strength of the CH_4 Q branch peak at 3022 cm^{-1}. As mentioned previously, the calculations for the error bars in Figure 3-6 are explained in Appendix C. The equation for the least squares linear fit is:

$$C_{CH_4} = 0.613 \cdot A(\nu_{CH_4}, peak) - 0.0003 \qquad (9)$$

As with the CO_2 correlation, the calibration appears reasonable because the low x intercept is close to zero, and falls within the error estimates for the measurement. As a comparison, the calibration curve for CH_4 is also computed using the area under the entire CH_4 band. Figure 3-7 shows calibration data and the least squares fit based on the area under the Q branch. While the fit of concentration versus area under the band is also good, it contains more scatter than method based on Q branch amplitude.
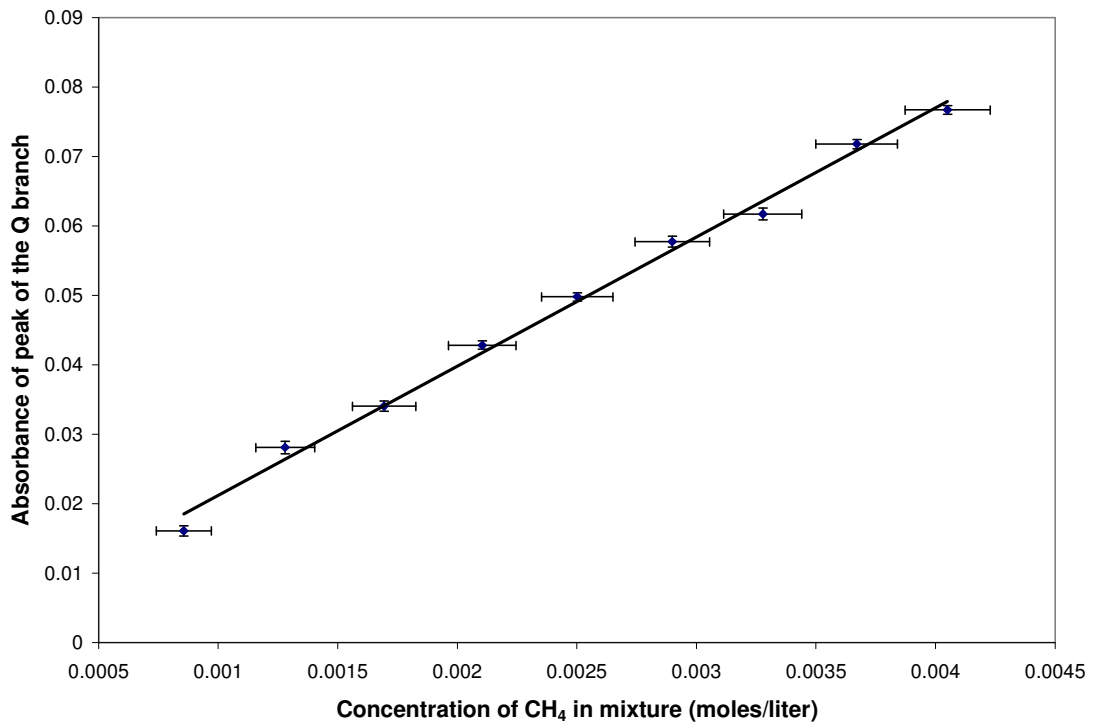
Figure 3-6: CH$_4$ calibration line for 2.15 mm wafer spacing
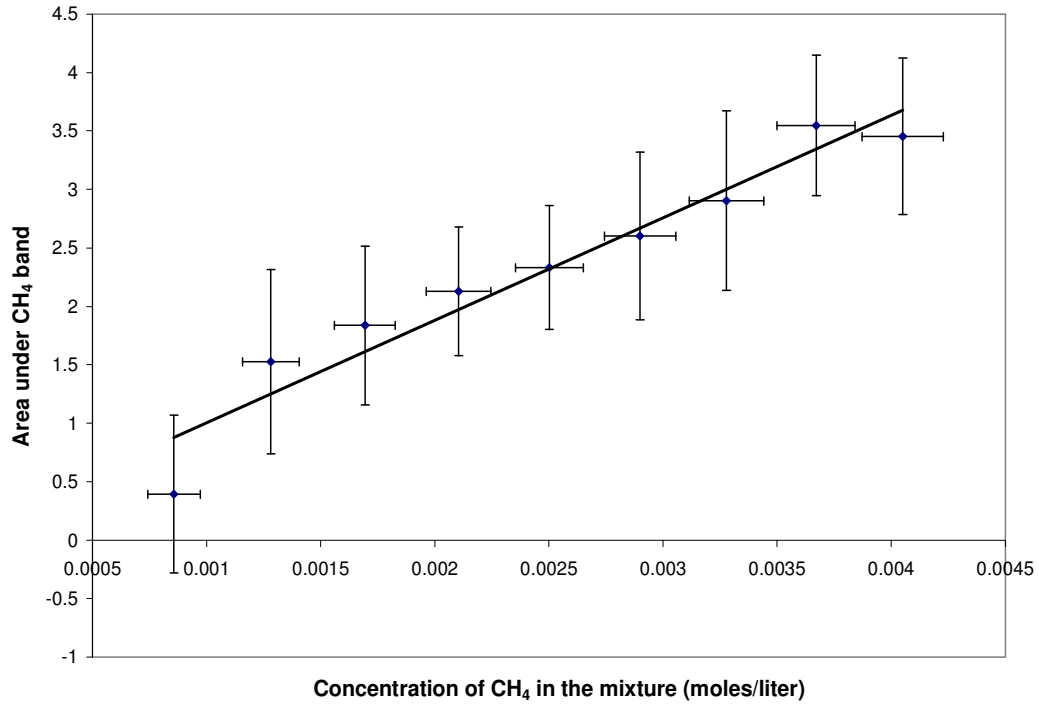
Figure 3-7: Calibration line for CH₄ concentration using the area under the band

3.3 – Method for Measuring Temperature

3.3.1 – Line By Line Spectral Models

The calculation of temperature or concentration of a molecular species from its absorption spectrum requires a model for molecular absorption. Basic molecular theories like the harmonic oscillator and rigid rotor approaches provide relatively reliable models for simple, 'well-behaved' molecules such as CO and CO_2 [33]. However, aggregate model approaches such as a line by line or wide band models [34] may be more useful in this application since these combine theory with experimental measurements. Both wide band models and line by line models can be used to make accurate measurements of temperature and concentration from IR absorption spectra [25-27].

Line by line calculations of the absorption spectrum are accomplished by looking at the individual transitions in a vibrational band and calculating the line strength based on the broadening coefficients, pressure, temperature, and molecular composition of the gas. Values for many of these molecular constants are available in the literature [35]. The most popular databases that tabulate this information are HITRAN and HITEMP [36, 37]. The HITRAN spectroscopic database has data for 38 different molecules that includes line strengths, broadening half widths, etc, corresponding to all of the various isotopes and transitions of each molecule. HITRAN data are very accurate at room temperature conditions. However the broadening half widths, and in particular the air-broadened half widths, are not well characterized at high (combustion) temperatures because they come from models and are not experimentally determined. HITEMP contains updated parameter values for CO_2, CO, and CH_4 at 1000 K, and includes rotational transitions that are only excited at elevated temperatures; hence HITEMP is more accurate at high temperatures. Data from the HITRAN/HITEMP databases can be used to construct a line-by-line model of an entire spectrum with molecular concentration, pressure and temperature as parameters. This model can then be fit to an experimental spectrum to determine temperature and concentration. This method is potentially very accurate since many points are required to achieve an accurate fit. It turns out, however, that the data in HITEMP is not accurate for temperatures much greater than 1000 K as shown by Modest [30]. As a result, it can be difficult to use line-by-line spectral analyses to determine gas temperatures and species concentrations accurately when the species being probed is not a diatomic molecule with relatively simple models for the

rotational and vibrational spectral structure. In addition, atmospheric pressure linewidth ($\sim$0.2 cm^{-1}) may result in significant undersampling using typical FTIR spectrometers with resolution on the order of 0.1 cm^{-1}, which makes application of line by line models problematic.

3.3.2 – Wide Band Spectral Models

Wide band spectral models simulate the temperature and concentration dependence of a molecule's vibrational absorption spectrum and have been used extensively for making in situ combustion measurements [24, 25, 28]. These models which were developed to accommodate older spectrometers that did not have adequate resolution to observe rotational features ($\nu > 0.05$ cm^{-1}), simply, consider the overall band structure of the molecule instead of the individual transitions. While there are many different wide band models, most like Fascode [38, 39] and Lowtran [38] were developed for interpreting atmospheric spectra. Radcal [40] and EM2C [41] were specifically developed for interpretation of spectra at flame temperatures. Wide band models are useful in measuring high temperatures and Modest [30] showed that wide band models are more accurate than fitting to the current line by line databases (such as HITRAN or HITEMP) for determining elevated temperatures from molecular spectra. Wide band models provide the only practical temperature measurement method in this work because (as will be discussed later) the signal strength is too low to measure CO absorption and as discussed above, the maximum resolution of the FTIR (0.1 cm^{-1}) is inadequate to resolve the individual rotational lines of CO_2.

In this work, EM2C was used to infer temperature from the CO_2 spectra. It can also be used to calculate the radiative intensity and transmissitivity of a nonisothermal and nonhomogenous mixture column of H_2O, CO_2, CO, and transparent gas-particles. This is accomplished by discretizing the path into n homogeneous and isothermal elements and using the Malkmus statistical narrow band model [42] and the Curtis-Godson approximation [43] over a spectral interval of 25 cm^{-1}.

The Malkmus model uses the conditions of Lorentz line shapes averaged over a wide spectral interval or a homogenous and isothermal column of absorbing gas. For a given length L (cm), total pressure p (atm), and molar fraction x of the considered absorbing gas, the transmissivity averaged over a Δv wide spectral range is:

$$\bar{\tau}(\Delta v) = \exp\left[-2\frac{\gamma}{\delta}\left(\sqrt{1 + xpLk\frac{\delta}{\gamma}} - 1\right)\right]$$ (10)

where k (in cm^{-1} atm^{-1}) and $1/\delta$ (in cm) are the model parameters that depend on temperature. γ (in cm^{-1}) is a typical collisional half-width of the lines of absorbing molecule. The parameters k and δ, which only depend on temperature T, are tabulated for a set of spectral intervals, Δv wide, centered in v_k. The EM2C model uses data from the Hitran database supplemented with proprietary data for the model parameters for k and δ. The collisional half-width for CO_2 is computed by:

$$\gamma_{CO_2} = \frac{p}{p_s}\left(\frac{T_s}{T}\right)^{0.7}\left[0.07x_{CO_2} + 0.058(1 - x_{CO_2} - x_{H_2O}) + 0.1x_{H_2O}\right]$$ (11)

where p_s is 1 atm and T_s is 296 K, p is pressure of the absorbing gas, T is temperature of the absorbing gas, and x_f is the mole fraction of given species f in the absorbing gas. The Curtis-Godson approximation consists of using Equation 10 to compute the transmissivity of a gas column by averaging k and (γ/δ) along the column.

3.3.3 - Technique

The populations of the various rotational bands change significantly with temperature, and this property is used to infer gas temperature from CO_2 spectra recorded by the FTIR and the wide band models for the spectra described in the previous section. In Figure 3-8, the change in the shape of the vibrational band caused by changing the temperature is shown. The hot CO_2 spectrum at 1450 K is broader because more of the higher energy rotational states are populated.

A fitting procedure is used to find the temperature of the spectra. A MATLAB least squares fitting routine, 'lsqcurvefit' based on a Newton-Gauss algorithm was used to find the best fit of the experimental spectrum using temperature as the fitting parameter. The fitting routine calls a Fortran program (included in Appendix A) that contains the EM2C wide band model. The routine begins with an initial guess for the temperature and concentration of CO_2, and calculates residuals based on the difference between the experimental spectra and the theoretical model.

The fitting routine then perturbs the values slightly to find the largest gradient for the input parameters of temperature and concentration and uses the direction of the gradient to iterate forward to find the best fit to the experimental spectra. The

temperature of the theoretical spectrum which best fits the experimental spectrum is assumed to be the gas temperature. Due to the mismatch in spectral resolution (EM2C is at 25 cm^{-1} resolution while the experimental data has 16 cm^{-1} resolution), the output of the EM2C model is interpolated to correspond to the experimental points. This is necessary in order to calculate the residual of the two spectrums. Additional details of the fitting procedure and the challenges involved in obtaining accurate fits are discussed in the next chapter.
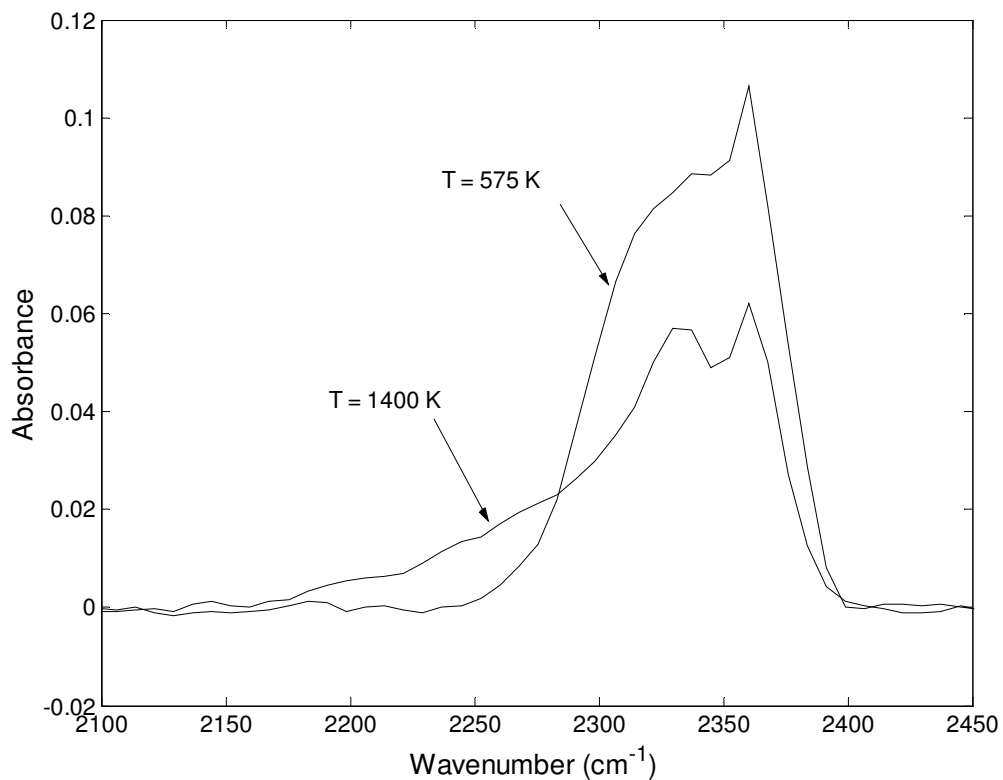
Figure 3-8: Broadening effects on CO_2 absorption signature

Chapter 4 – Challenges

4.1 – Interference from Silicon

Figure 4-1 shows a typical spectral fit performed using the routine described in the previous chapter. The fit gives a gas temperature of 791K with an R^2 value of 0.872 which is quite low. One reason for the poor correlation is that the EM2C fit does not match the dip at the top of the band shown in the experimental spectrum. The reason is that the 'dip' arises from interference from the silicon wafer and not from an absorption feature of CO_2.
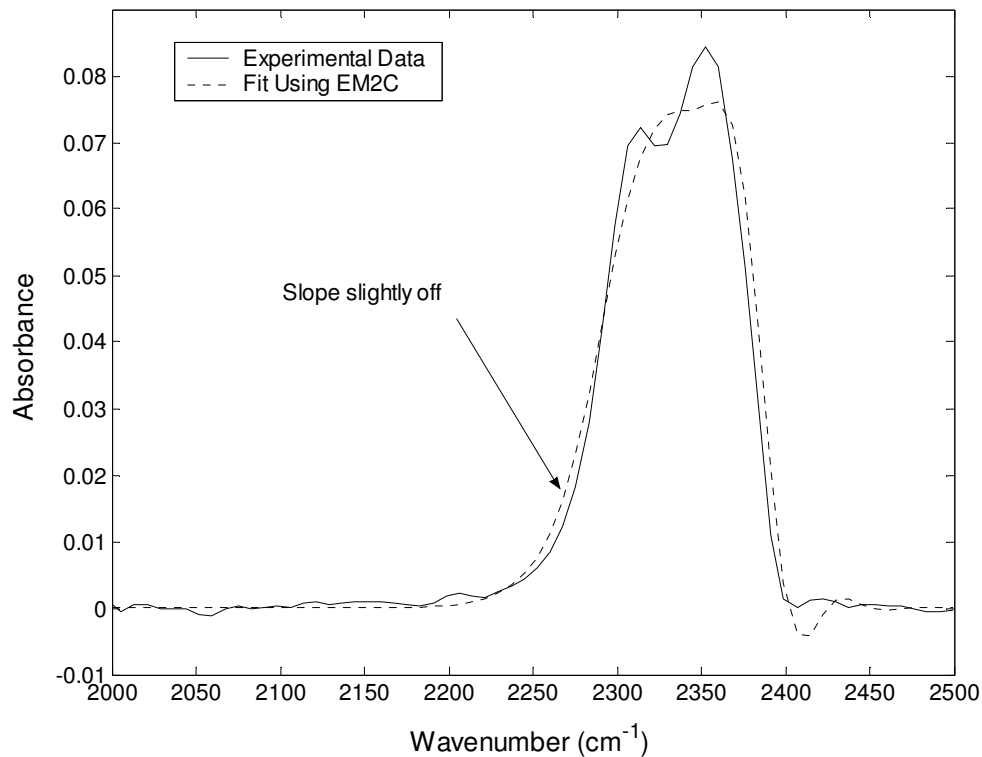
Figure 4-1: Fit of CO_2 spectra with EM2C model

Figure 4-2 is a higher resolution measurement of the silicon interference at two different temperatures. Note that it is a strong function of temperature. This

temperature dependence corrupts the fitting procedure in this region because

variations in the transmissivity of silicon are not included in the spectral model. The

cause of this absorbance is not clear, though it could possibly be related to light

scattering by dopants or may be an etaloning effect.
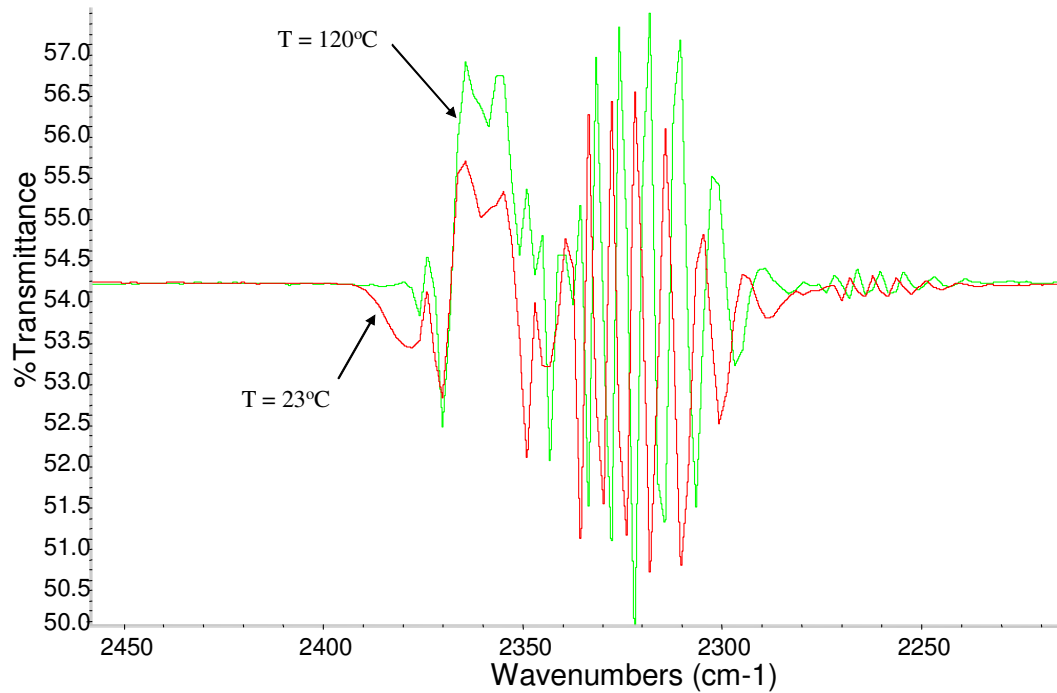
Figure 4-2: Change in interference on the CO_2 band in silicon wafer with temperature at 4 cm^{-1}

resolution

Figure 4-3 shows that the problem is much more serve when the spectrum is

acquired at 4 cm^{-1} resolution.
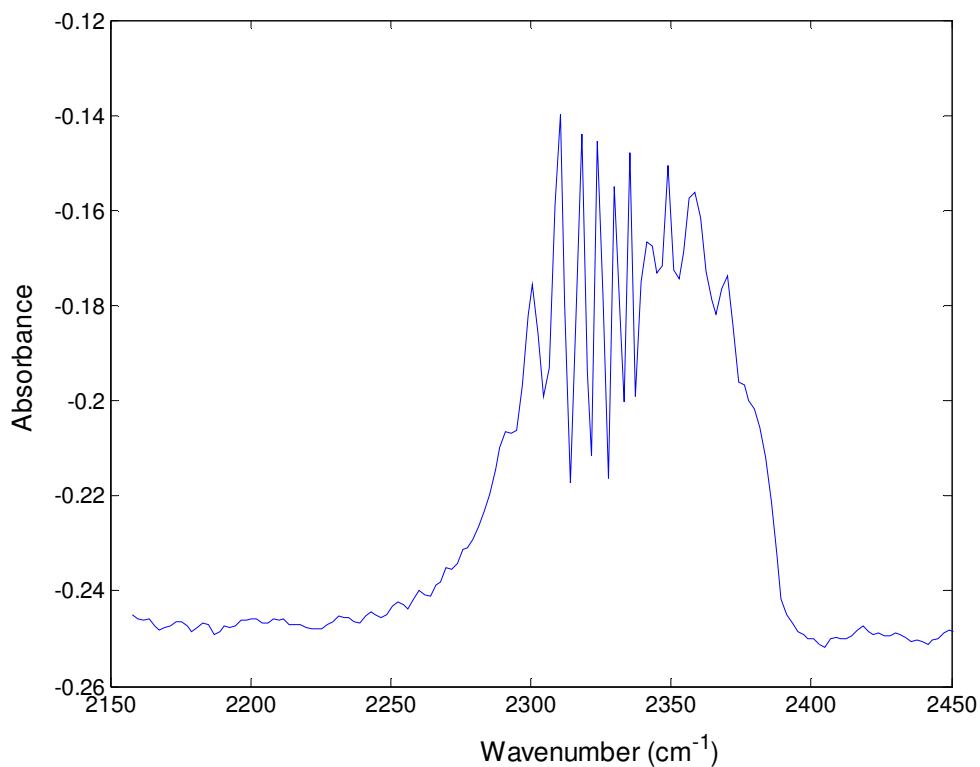
Figure 4-3: Typical interference on CO_2 band at 4 cm^{-1}

At 16 cm^{-1} resolution, however, the spectral averaging results in a fit that is slightly off in the region between 2150 and 2300 wavenumbers where CO_2 broadens due to temperature.

The solution to the interference problem is to retain the 16 cm^{-1} resolution and fit only the region from 2150 – 2300 cm^{-1} to determine temperature, avoiding the spectral region with the interference. Figure 4-4 shows the fit using only this region. The new temperature is 660 K and has an R^2 value of 0.996, which indicates a very strong correlation.
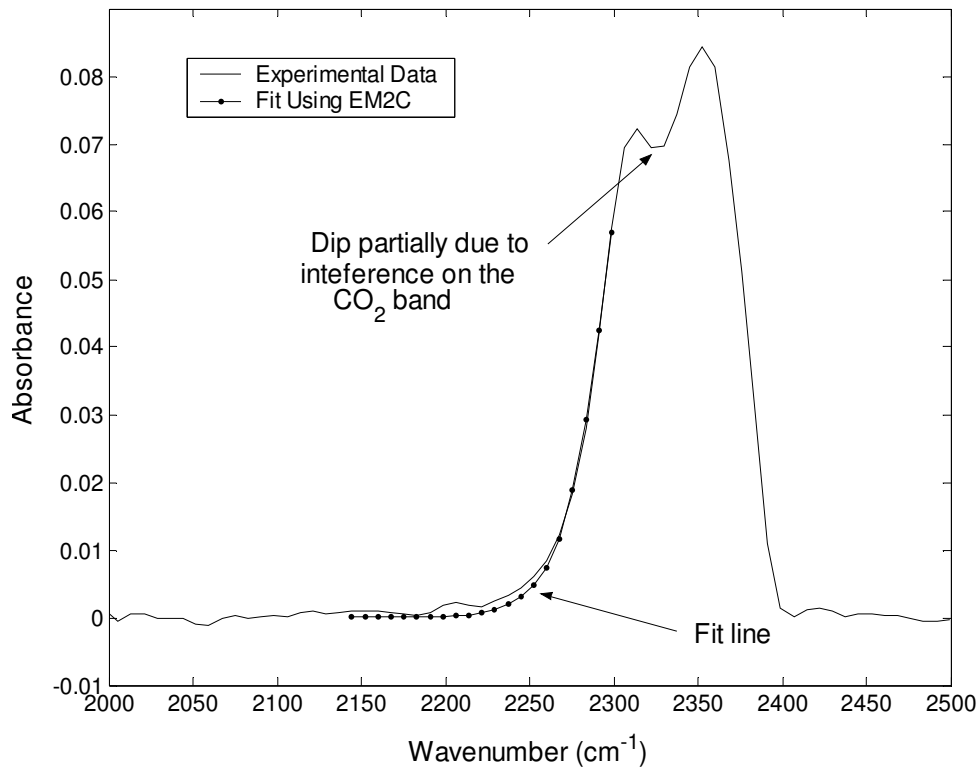
Figure 4-4: CO_2 spectra with fit only in region of 2150-2300 cm^{-1}

4.2 – Signal Strength

4.2.1 – Temperature Dependence of Silicon Transmissivity

The transmittance of high purity silicon wafers has been shown by Runyan to

decrease with temperature [44]. This can have negative effects on the temperature

and concentration measurements by reducing the signal to noise ratio at high

temperatures. To test this, the silicon walls of the burner were heated with a heat gun

to various temperatures and spectra were acquired to see how the transmittance

changes with temperature. The temperature of the wafer was measured using a

sheathed K type thermocouple in mechanical contact with the front wafer surface at a

point immediately adjacent to the optical interrogation region. Since silicon a very

high thermal conductivity, the Biot number was assumed to be low and the region interrogated by the beam was assumed to be at an approximately uniform temperature. Figure 4-5 shows the temperature dependence of the transmittance of the double side polished wafer at 2600 cm^{-1} measured in the silicon-walled burner. There is significant scatter in this data because readings of the wafer temperature using the thermocouple pressed against the surface of the wafer were rather inaccurate due to variations in the contact resistance. The solid line drawn through the data points in this figure is a best fit polynomial curve.

Figure 4-5 shows that the transmittance drops dramatically for temperatures greater than about 300 C. The transmittance in the spectral region covering the CH$_4$ and CO$_2$ bands (2100-3200 cm^{-1}) is not shown but varied in a similar manner. Since at least 4% transmission is required to get an acceptably low signal to noise ratio, Figure 4-5 indicates that the temperature of the silicon walls must be lower than 400°C in order to make measurements.

4.2.2– Etaloning

Another important challenge is self-interference of the interrogation beam caused by multiple reflections off the various surfaces of the wafer. Spectral measurements made when the burner walls were constructed from two double polished silicon wafers showed fringe patterns similar to those produced by a Fabry-Perot etalon [45]. This sinusoidal pattern can be seen in plots of the intensity of the FTIR beam vs. wavelength (Figure 4-8).
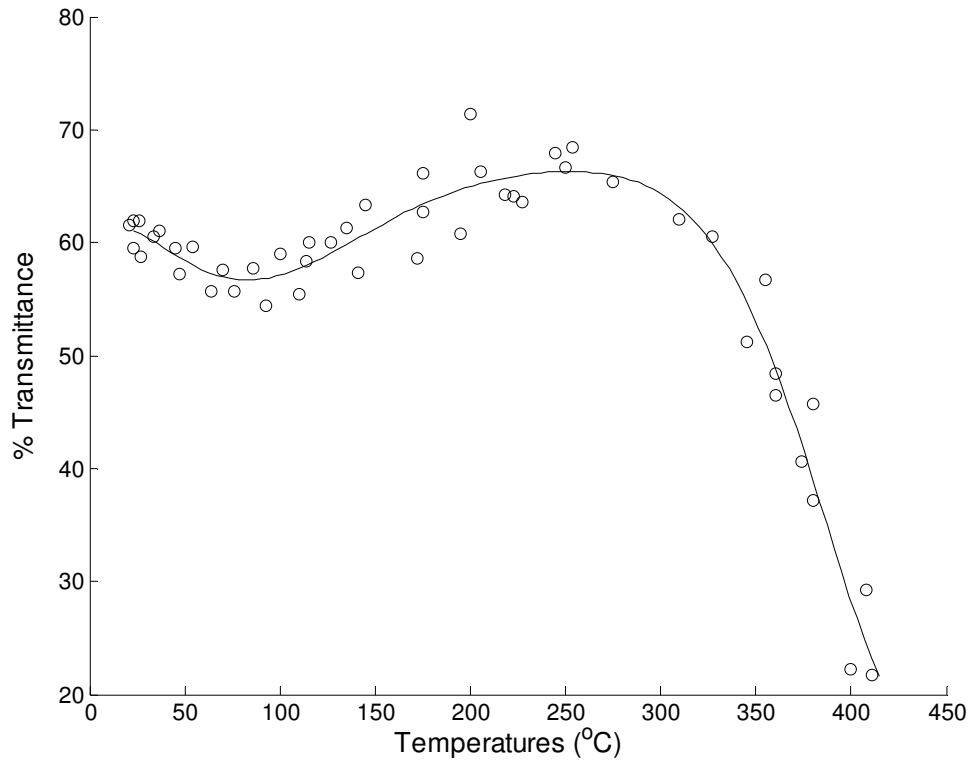
Figure 4-5: %Transmittance of double side polished Si wafer vs temperature at 2600 cm^{-1}

Fabry-Perot etaloning occurs when a beam undergoes multiple reflections and transmissions off a surface as illustrated in Figure 4-6.
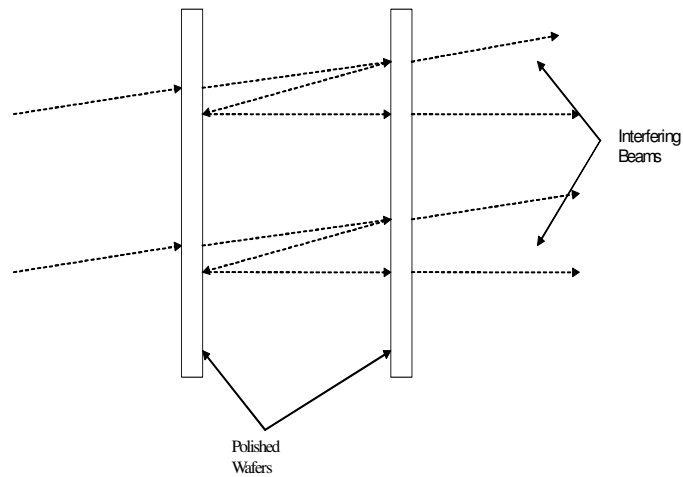
Figure 4-6: Diagram of etalon effect

The interference is related to the difference in path length of the reflected and transmitted beam. This can be described by the 'Airy function' [45]:

$$\frac{I}{I_0} = \frac{1}{1 + F \sin^2\left(\delta/2\right)}$$

(12)

$$F = \frac{4R}{(1-R)^2}$$

(13)

$$\delta = \frac{2\pi}{\lambda} n'h \cos\theta$$

(14)

where h is the plate thickness, n' the plate index of refraction, θ the incident angle of the light, λ_0 the wavelength of incident light, and R the wafer reflectivity. Figure 4-7 shows plots of the Airy function corresponding to two wafer temperatures. The reflectivity is assumed to be constant at 0.3 as is the index of refraction at 1.45. The temperature dependence enters through the plate thickness h and the coefficient of thermal expansion (CTE) for silicon. While this is also a function of temperature, for the purposes of this basic demonstration it is assumed to be a constant 3e-6 K^{-1}. The two fringe patterns shown in Figure 4-7 correspond to a temperature difference of 200K. Since the shift of the temperature-induced shift in the Airy fringe pattern is similar to the shift in the fringe pattern observed experimentally in Figure 4-8, we can conclude that this pattern is the result of etaloning.
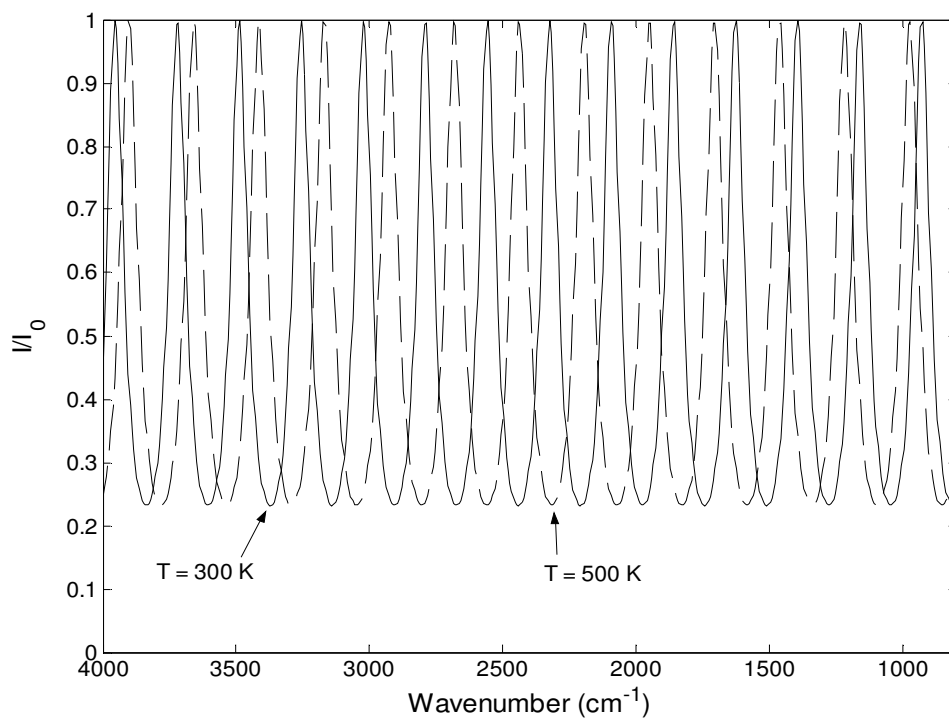
Figure 4-7: Airy function showing the interference shift for two temperatures
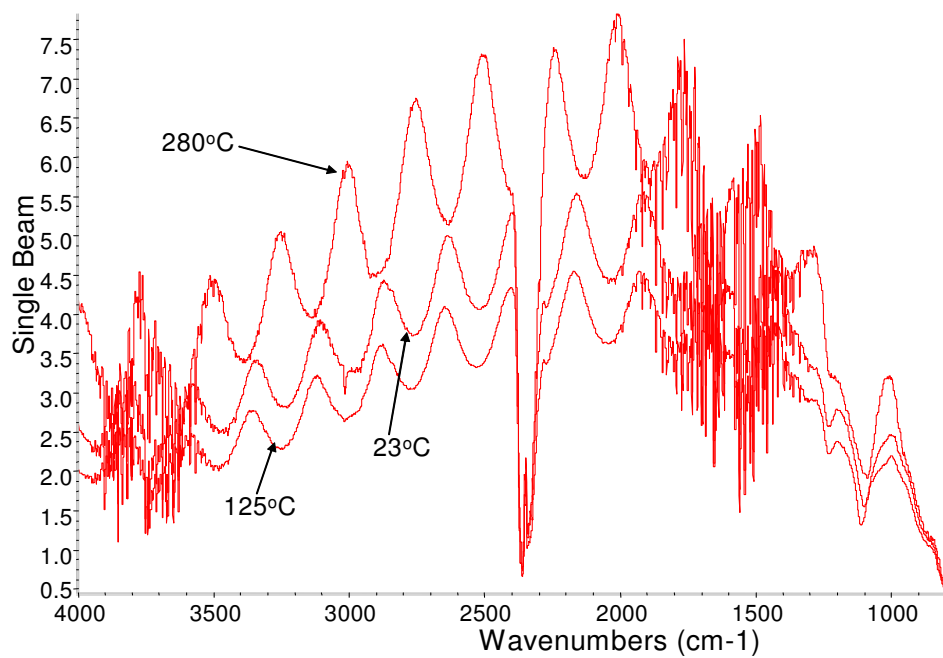
Figure 4-8: Shift in interference fringes for several temperatures

41

Ordinarily, this pattern would not affect the final absorbance measurement because the absorbance is computed using the ratio of the transmitted intensity during the experiment to a reference intensity corresponding to zero absorption. This is measured at room temperature with only air (no reactants or products) in the burner and accounts for losses in the optical system. If these losses change with temperature, however, there is no way to determine the appropriate reference intensity by which to normalize the transmitted signal. As a result, the etaloning effect makes it impossible to determine the proper absorption spectrum and thereby makes it impossible to determine temperature or concentration accurately.

To prevent the etaloning effect from occurring, a single side polished and a double side polished wafer are used in combination as illustrated in Figure 4-9. The single side polished wafer acts as a diffuser and disrupts the interference by randomizing the angles of reflection of each incident ray. Unfortunately, the reduction in signal intensity is dramatic, as the single side polished plate only transmits 5% of the incoming light, compared with 60% for a plate with both sides polished. The single side polished plate is placed on the far side of the path to make sure that the beam is only scattered after passing through the interrogation volume.

4.2.3– Spatial Resolution

Tradeoffs between source coherence and source strength made it difficult to achieve high throughput and spatial resolution less than 1 mm in the flow direction. The light source in the Nexus 870 is a resistively heated element that is approximately 1 cm tall and is held at a constant temperature to ensure that its emission spectrum remains constant. The relatively large size of the source causes

the spatial coherence of the beam to be low and produce a beam that is very divergent and diffusive. This, in turn, makes it difficult to focus the beam in a well-defined point. The spatial coherence of the source can be adjusted using an aperture in the FTIR.
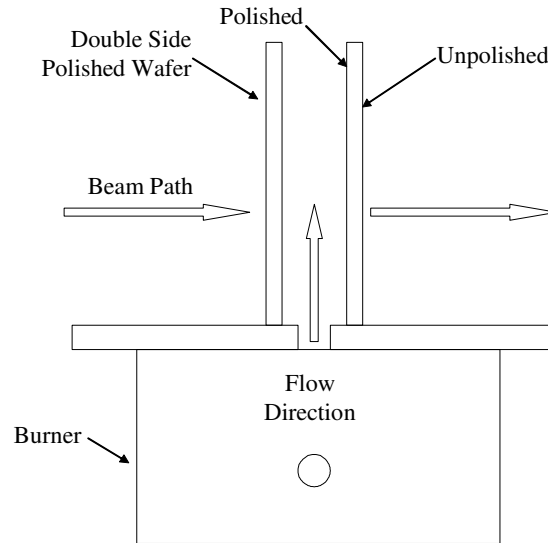
Figure 4-9: Arrangement of wafers in burner to eliminate etaloning

This aperture can be reduced in steps from fully open (~1 cm) to approximately 1 mm in diameter. Reducing the aperture improves the spatial coherence but reduces signal strength by a factor of $1/r_a^2$, where r_a is the radius of the aperture. After experimenting with several apertures, it was concluded that a mask would be used to block the beam as it enters the burner and the aperture would be left fully open. A rectangular mask that is 1 mm wide in the streamwise direction but 8 mm wide in the spanwise direction was used to maximize spatial resolution in the streamwise direction while allowing the maximum possible amount of light through.

Chapter 5 – Results

5.1 – Temperature Measurement

The spectral temperature measurement method is used to measure the change in temperature as a function downstream distance in the micro-burner. This information can be used to compute the heat loss, the combustor thermal efficiency, and the flame thickness. The temperature as a function of downstream distance for CH_4-air combustion with $\phi = 0.86$ and a flow speed of 44 cm/s is shown in Figure 5-1. Note that there is not enough CO_2 in the measurement to determine the temperature there. The error bars are larger on the first few points in Figure 5-1 due to the fact that the CO_2 concentration is small because it is still being produced. This reduces the signal to noise ratio and thereby increases the uncertainty. The peak temperature measured is 1427 K and the temperature falls in the downstream direction as expected.

Note that the uncertainty of the first measurement point is extremely large. This arises because of a problem with the fitting procedure at very high temperatures. Figure 5-2 shows the fit for temperature for a spectrum acquired 20 mm downstream of the burner entrance. The wafer spacing is 2.15 mm, the equivalence ratio is 0.86, and the flow speed is 44 cm/s. This measurement location is immediately downstream of where the CO_2 spectrum is very broad because of the high temperature. The fitted temperature is 1400 K ±88 K. The large uncertainty is due to the influence of the spectral wings: the broadening of CO_2 pushes a larger portion

of the absorption feature into a region where the absorbance is small and the signal to

noise ratio is low.
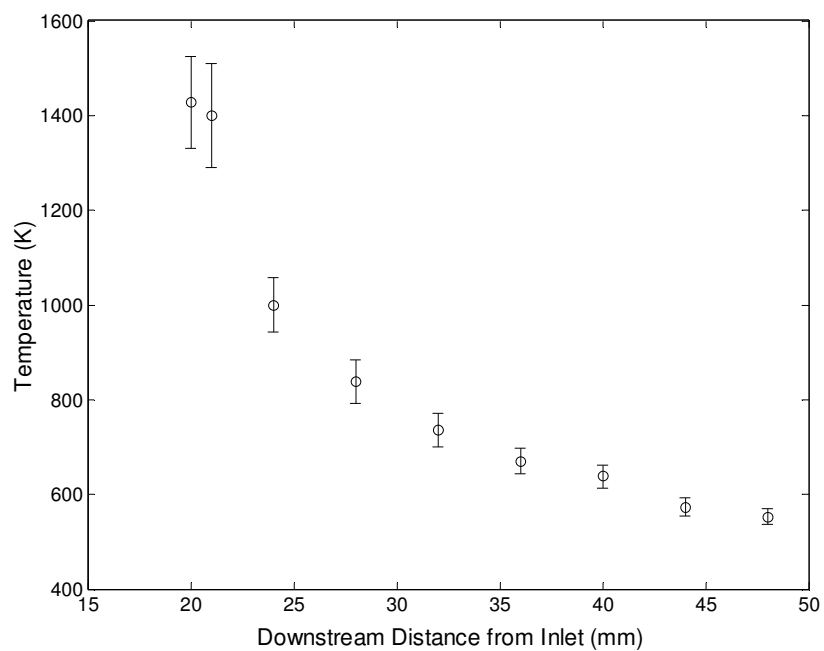
Figure 5-1: Temperature vs. distance downstream from the inlet in the post flame: $\phi = 0.82$ U = 44 cm/s
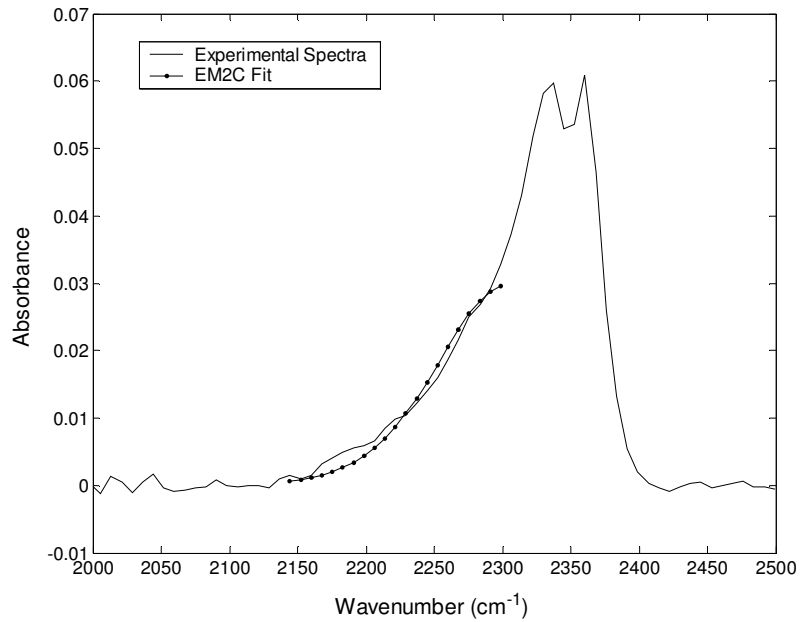
Figure 5-2: Fit of high temperature CO_2 spectrum: ϕ = 0.86 U = 44 cm/s, 2.15 mm wafer spacing, 20 mm downstream from the inlet

As a quality check, model spectra for temperatures ±120 K about the fitted temperature are plotted in Figure 5-3 along with the fit. The figure clearly shows that the fit corresponds best to the experimental spectra. The fit matches the experimental data best on the slope of the CO_2 wing where the high temperature features are located.

47
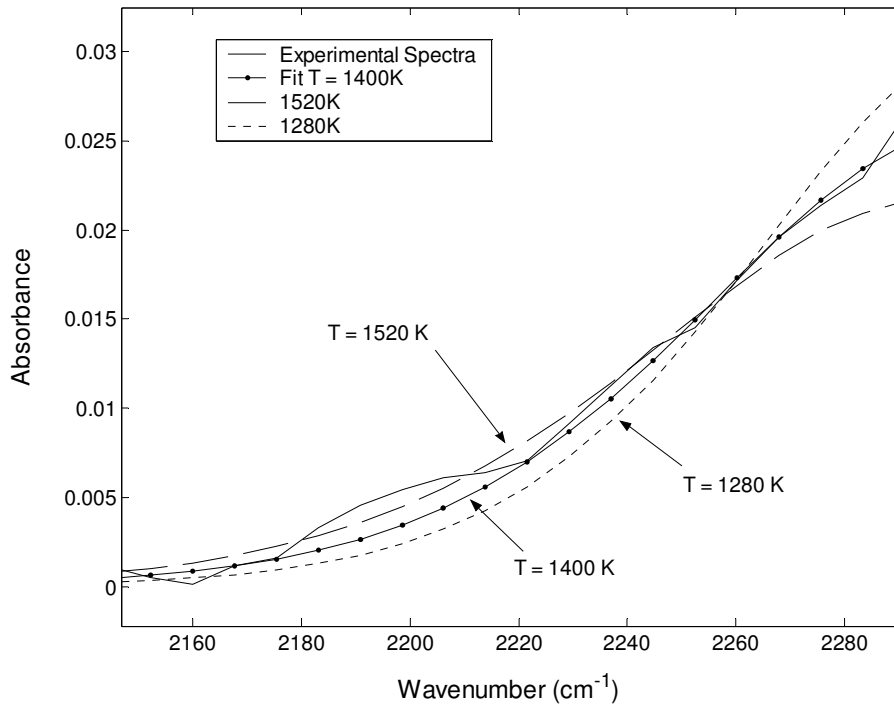
Figure 5-3: Comparison of spectral fit at 1400K to model spectra corresponding to ±120 K. ϕ = 0.86 U = 44 cm/s, 2.15 mm wafer spacing, interrogation region location: 20 mm downstream of the inlet.

On several of the points in Figure 5-1 the uncertainty is calculated to be less than 30 K. These points correspond to spectra where the signal to noise ratio is slightly larger and the fit is excellent. For example, Figure 5-4 shows the spectrum at the point 40 mm downstream from the inlet, where the temperature is measured as 637 K with an uncertainty of ±22 K. The fit is very good along the CO_2 band, as compared to the fit previously shown in Figure 5-2. Figure 5-5 shows the quality of the fit for Figure 5-4 by comparing the fit at 637K to model spectra computed at ±50 K.
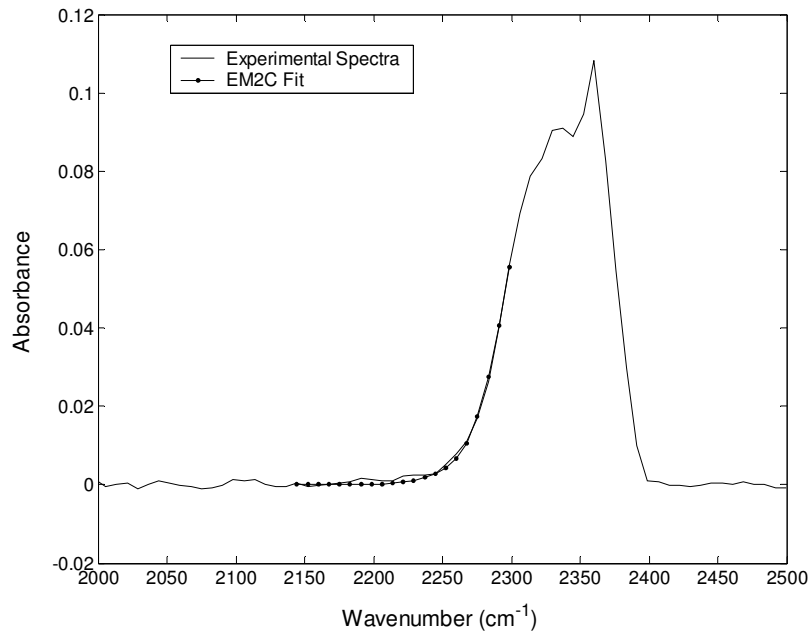
Figure 5-4: Fit of CO_2 band: 40mm downstream from the inlet, $\phi = 0.86$, U = 44 cm/s, 2.15 mm wafer spacing, interrogation region 40 mm downstream of inlet.
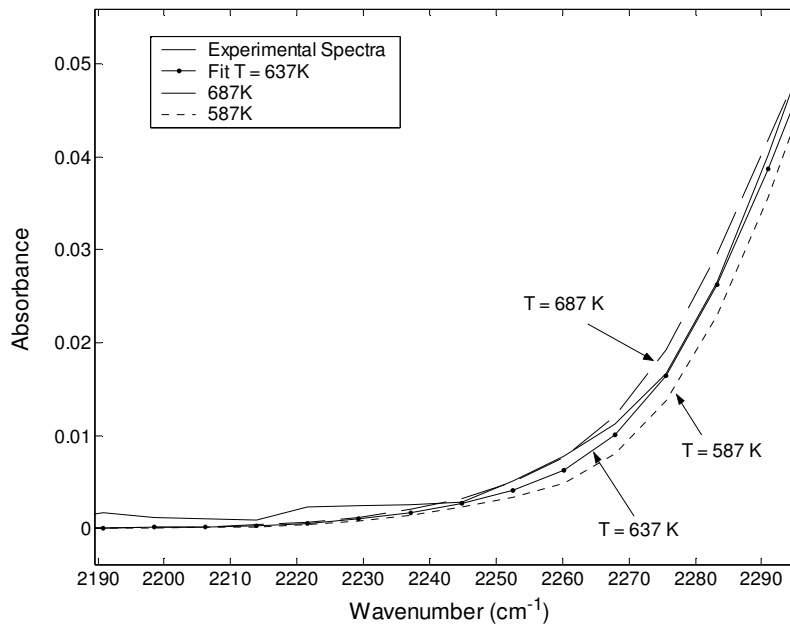
Figure 5-5: Comparison of spectral fit at 637K to model spectra at ± 50 K. $\phi = 0.86$, U = 44 cm/s, 2.15 mm wafer spacing, interrogation region 40 mm downstream of inlet.

5.2 – Comparison of Spectral and Thermocouple Measurements

Gas temperature measurements made using the fitting method were compared to those made using an Omega 0.01" diameter k-type ungrounded thermocouple with a stainless steel sheath. The thermocouple was placed in the beam path between the silicon wafers to find the gas temperature at the FTIR interrogation location. A flame was stabilized on the bottom of the burner so that the thermocouple was in contact with low temperature post flame gases. This prevented damage to the thermocouple. The burner was raised so that spectra and thermocouple measurements could be acquired at different positions in the exhaust.

Thermocouples must be corrected for heat loss to find the true gas temperature from the measured thermocouple temperature. The correction is determined by performing an energy balance on the thermocouple bead:

$$\dot{Q}_{conv} + \dot{Q}_{cond} + \dot{Q}_{rad} + \dot{Q}_{cat} = 0 \tag{15}$$

In this expression $\dot{Q}_{conv}$ is the convective heat transfer of the gas flow to the thermocouple, $\dot{Q}_{cond}$ is the conductive heat transfer of the thermocouple sheath, $\dot{Q}_{rad}$ is the radiative heat transfer of the thermocouple to the surrounding environment, and $\dot{Q}_{cat}$ is the heat generated by any catalytic reactions on the thermocouple's surface. In this case, catalysis is neglected because the thermocouple sheath was made of relatively unreactive stainless steel. Equation 15 can be rewritten as:

$$h\left(T_{gas} + T_{TC}\right) = \sigma\varepsilon(T_{TC}^4 - T_W^4) + k\left(\frac{dT_{TC}}{dx}\right) \tag{16}$$

where T_{TC} is the measured thermocouple temperature, T_{gas} is the gas temperature , T_w is the silicon wafer wall temperature, h is the heat transfer coefficient between the gas and the thermocouple bead, ε is the emissivity of the thermocouple bead, k_{TC} is the thermal conductivity of the thermocouple leads and sheath, and σ is the Stefan-Boltzmann constant. Incorporating the Nusselt number, defined as $Nu_d = \dfrac{hd}{k_{gas}}$, where d is the diameter of the bead and k_{gas} is the thermal conductivity of the gas, the gas temperature is found to be:

$$T_{gas} = \left[\sigma\varepsilon(T_{TC}^4 - T_W^4) + k(\frac{dT_{TC}}{dx}) \right]\frac{d}{Nu_d k} + T_{TC} \qquad (17)$$

Kramer's correlation for a cylindrical thermocouple gives the Nusselt number for this situation [46]:

$$Nu_d = 0.42\,Pr^{0.2} + 0.57\,Pr^{\frac{1}{3}}\,Re_d^{\frac{1}{2}} \qquad (18)$$

where Pr is the Prandtl number for the gas and Re_d is the Reynolds number based on the bead diameter. Table 1 summarizes the values of the parameters used in the thermocouple correction and Figure 5-6 shows how the thermocouple temperature correction varies axially through the flame. Note that the hotter readings require more correction as there is greater ΔT between the thermocouple and the environment and thus more heat is lost.

Figure 5-7 compares the corrected thermocouple measurements to the spectrally-based measurements. It shows that the thermocouple and spectral measurements agree with each other within their uncertainty boundaries. The uncertainty in the temperature measurement is determined by the quality of the fit,

rms noise, and the change of the shape of the band due to small changes in temperature. The calculation of uncertainty is discussed in greater detail in Appendix C, but it should be noted that the largest uncertainties in Figure 5-7 are caused by lower quality fits with R^2 values below 0.99. The uncertainty rises dramatically where the R^2 value falls below 0.99.

Table 1: Parameters used for thermocouple correction

Parameter	Value	Units	Reference
ε_{bead}	0.23		T= 800 K [47]
$k_{ss\ sheath}$	21.3	W/(m-K)	T = 800 K [47]
k_{gas}	0.051	W/(m-K)	air (T = 700 K) [48]
d_{bead}	0.01	in	
Pr	0.702		air (T = 700 K) [48]
Re_d	557		
Nu_d	12.2		
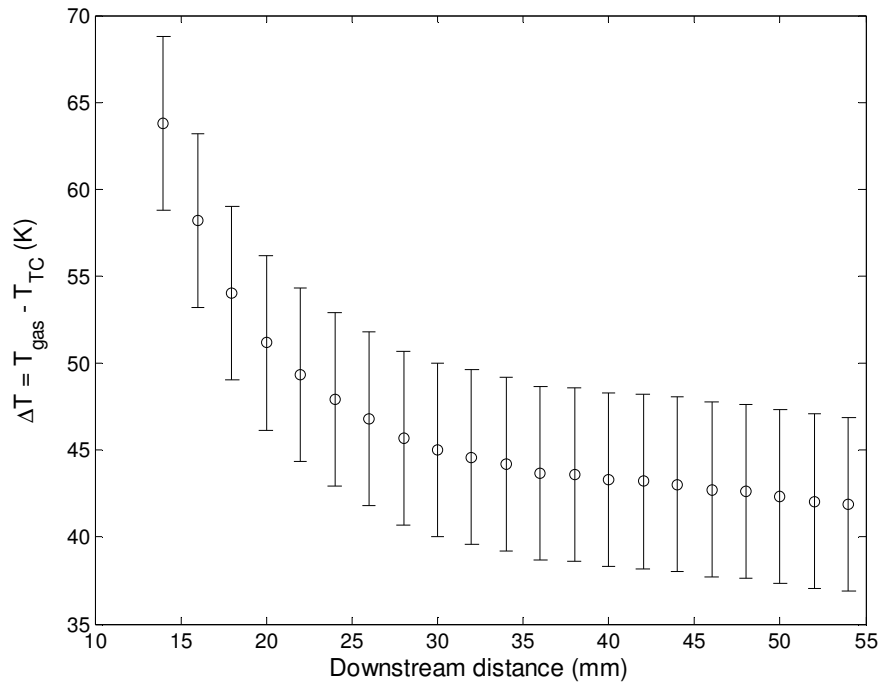
Figure 5-6: Temperature correction calculated for the thermocouple reading used to calibrate the temperature fitting routine

Another way to look at the calibration of the temperature fit is to plot the corrected thermocouple data versus the fitted temperature as shown in Figure 5-8. The linear least squares fit has a slope of 0.972 and an x-intercept of $19^{\circ}C$. The R^2 value of the linear fit is 0.998. Taken together, these indicate that the thermocouple and spectroscopic measurements are reasonably well correlated.
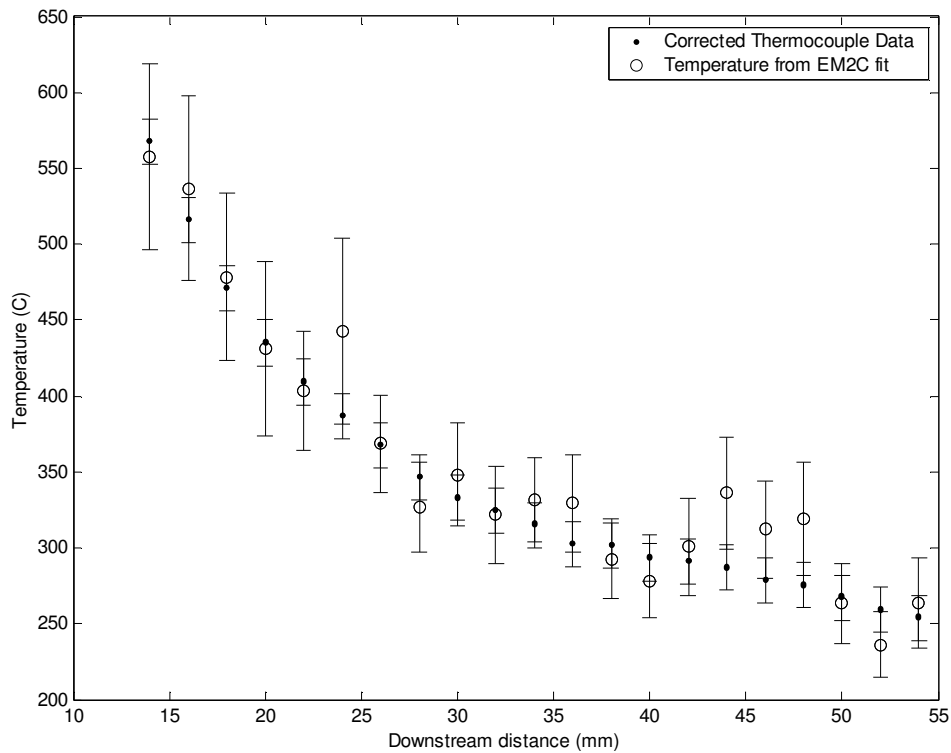
Figure 5-7: Comparison of axial temperature profiles measured using a thermocouple and computed using the CO$_2$ spectral fitting method
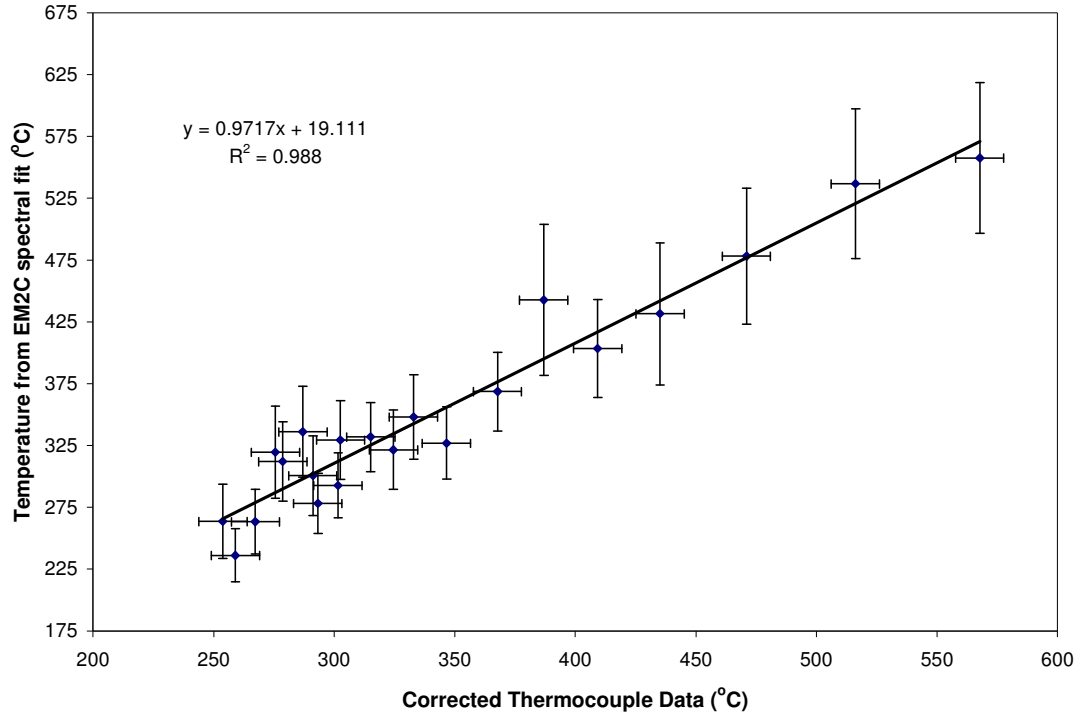
Figure 5-8: Corrected thermocouple data vs. temperature from EM2C fit

5.3 – Effects of Span-wise Discretization of the Optical Path

To this point, it has been assumed, that the gas temperature is constant across the beam path between the wafers in the determination of the spectral gas temperature. However, heat losses to the walls are expected to result in a parabolic temperature profile similar to the parabolic velocity profiles that characterize flow between two parallel plates (Poiseuille flow). If the temperature distribution in the gas is parabolic, the cooler gas at the walls would affect the overall gas temperature "measured" using the spectroscopic technique. To account for this effect, the path was discretized into 'n' uniform sections whose individual temperatures had the following parabolic distribution as a function of distance x between the plates:

$$T_{profile} = a \cdot x^2 - a \cdot x_{width} + c \qquad (19)$$

In this expression, a and c are the polynomial coefficients of the parabola and x_{width} is the plate spacing. Figure 5-9 is a schematic diagram illustrating how the beam path is discretized and the parabolic temperature distribution. The EM2C narrow band model can accommodate multiple beam paths so the fitting program was modified to vary the parameters a and c to find the best fit between the model and the measured spectrum. Note that the best fit for a and c enables the centerline temperature and the gas temperature near the wall to be found.

Discretized Parabolic Temperature Profile

Discretized Beam Path

Si Wafer
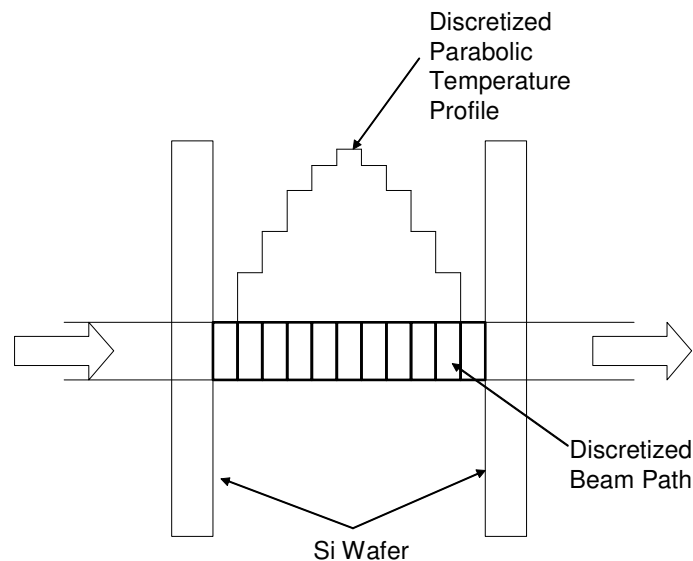
Figure 5-9: Schematic of beam path

As discussed earlier, Figure 5-2 is a good fit of the spectra but is slightly off. In Figure 5-10, the same spectrum is fit using a temperature profile discretized into 15 sections. The resulting fit is much better than that shown in Figure 5-2 because it captures the fact that the overall absorbance results from the combined effect of many samples at different temperatures. Figure 5-11 shows the discretized temperature profile for the CH_4-air flame at an equivalence ratio of 0.86. The centerline temperature is found to be 2106 K ± 156 K and the gas temperature near

55

the wall is 688 K. The centerline temperature is very close to the adiabatic flame

temperature of 2083 K for an equivalence ratio of $\phi = 0.86$. This is reasonable as

one would expect the flow along the centerline to have the least thermal contact with

the cooler walls.
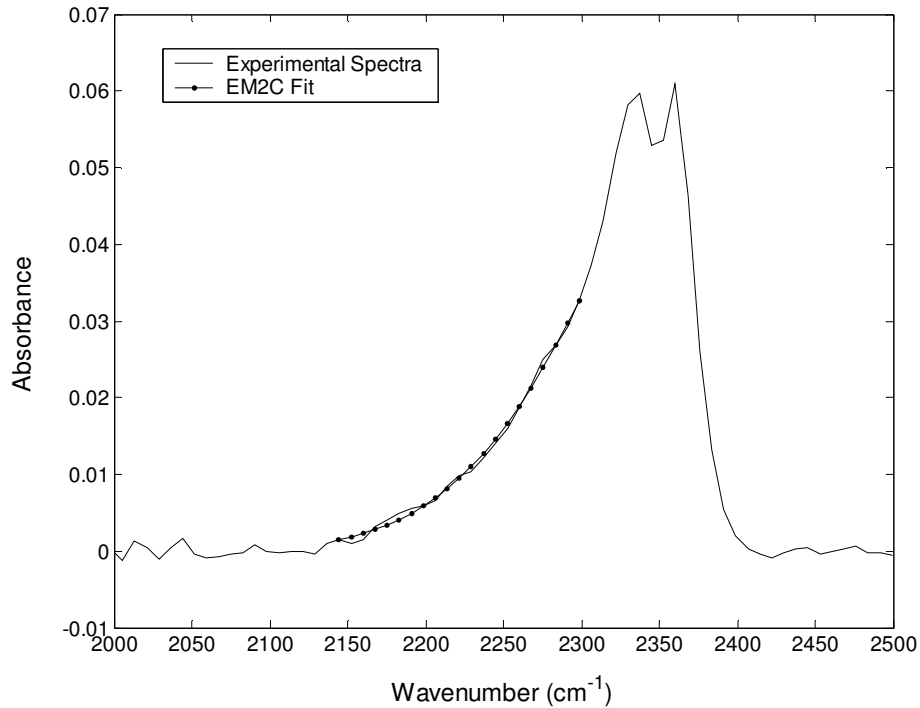
Figure 5-10: Fit of CO_2 spectra using 15 discrete sections for temperature profile: $\phi = 0.86$, U =

44 cm/s, 2.15 mm wafer spacing, 20 mm downstream from inlet

Since the division of the domain into 15 discrete sections appeared to

enhance the performance of the fit, the effect of the number of discrete sections on

the centerline and wall temperature was investigated. The results are presented in

Figure 5-12. They show that the centerline temperature initially increases as one

increases the number of cells, overshoots the adiabatic flame temperature, and then

converges to a constant value when the number of cells reaches 15.
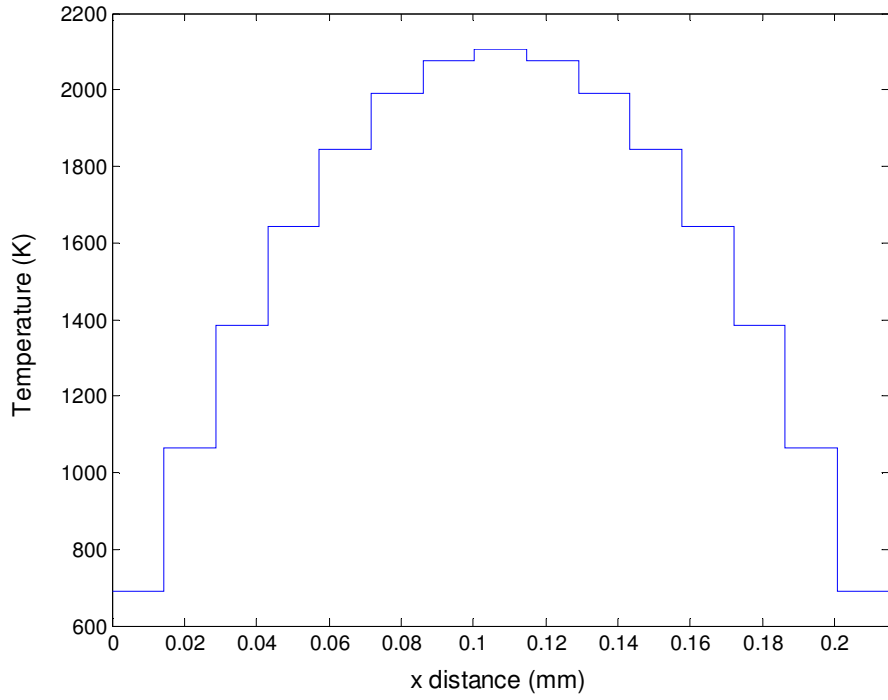
Figure 5-11: Discretized temperature profile for Figure 5-6
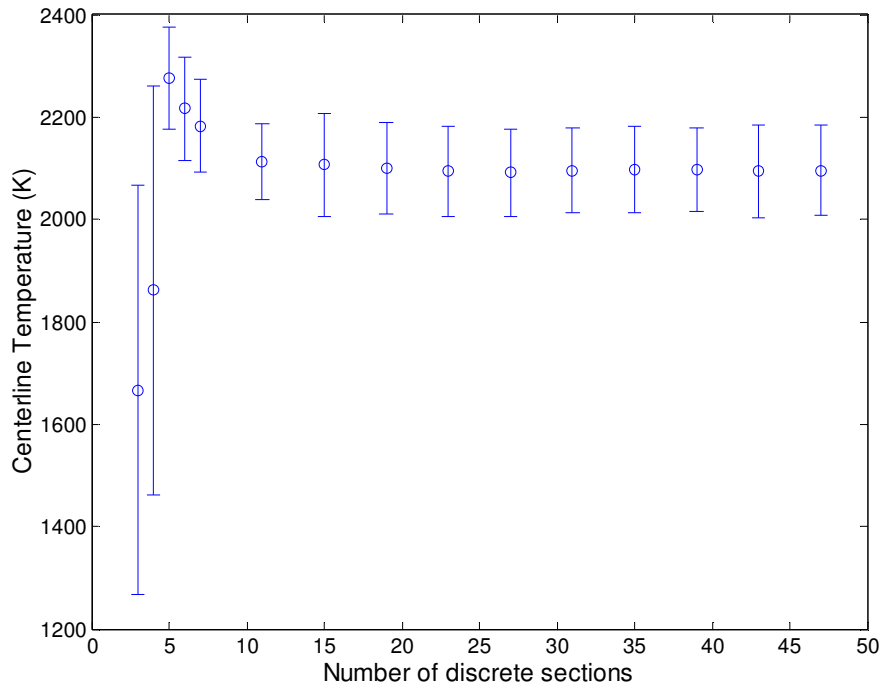
Figure 5-12: Affect of number of discrete sections on the centerline temperature

Figure 5-13 is a similar plot showing the effects of the number of sections on the gas temperature near the wall. It shows that the discretization of the path affects the results until approximately 35 sections, after which a relatively constant value is found. Based on the results for centerline and wall temperatures, approximately 35 sections appears optimal for minimizing the computational time while still getting reliable estimates for the gas temperatures near the wall and at the centerline.
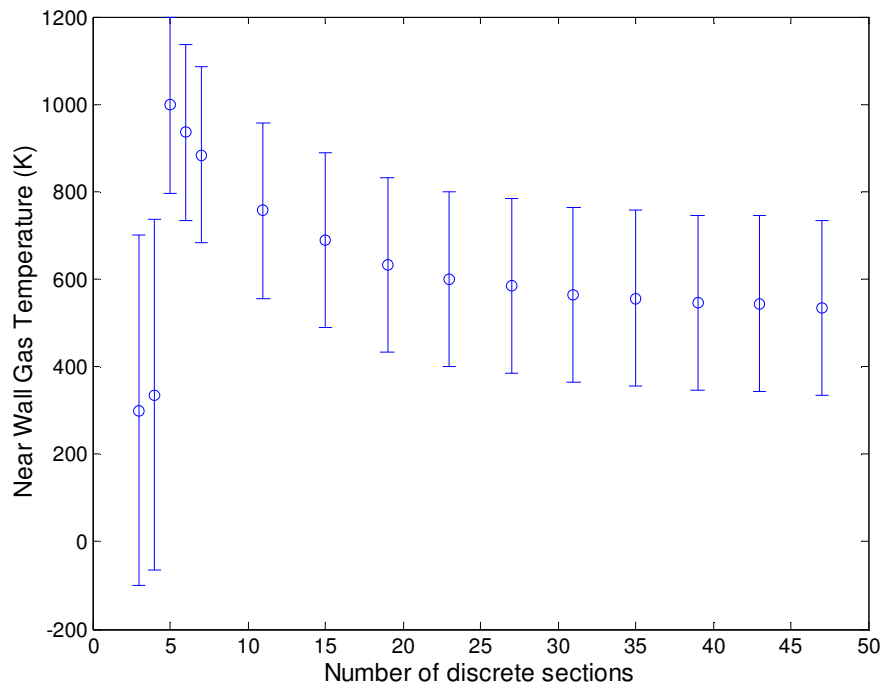
Figure 5-13: Effect of number of discrete sections on the gas temperature near the wall

Figure 5-14 shows how the single section temperature profile shown in Figure 5-1 compares with the gas temperature near the wall determined using 35 discrete sections for the fit. Note that the temperatures associated with the 35 section fit are consistently higher than those associated with the single section fit. The difference is greatest near the flame, since the temperature profile is far steeper there

than for cooler regions of the combustor. This is consistent with the earlier

comparison to thermocouple measurements in Figure 5-7. Figure 5-15 compares the

centerline temperatures determined using the 35 section fit to the corrected

thermocouple measurements. Note that the agreement is much better than that

shown in Figure 5-8. The slope is now 0.994 and the y intercept is $1.24^{O}C$ indicating

a very good correlation between the thermocouple and spectroscopic temperature

measurements.
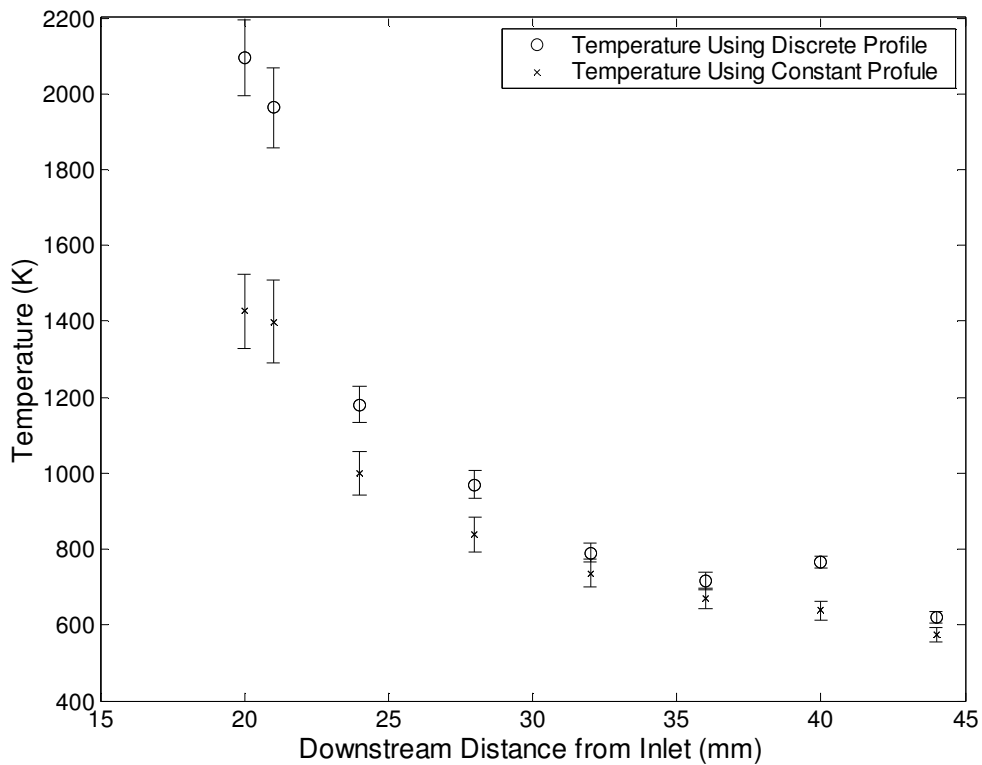
Figure 5-14: Comparison of temperature profiles using 35 discrete sections profile and constant

profile: $\phi = 0.86$, U = 44 cm/s, 2.15 mm wafer spacing

Figure 5-16 is a plot of the gas temperature near the wall found by the

discrete fitting for the same conditions in Figure 5-1. It shows that the near wall gas

temperature falls as expected with downstream distance. However, the uncertainty in the measurements is large because the fitting procedure is much more sensitive to the center section of the profile than the edges. This is because the highly excited high temperature states populated in the center section play a larger role in determining the final absorbance spectra. While a downward trend is perceptible the error bars indicate that it is not very reliable.
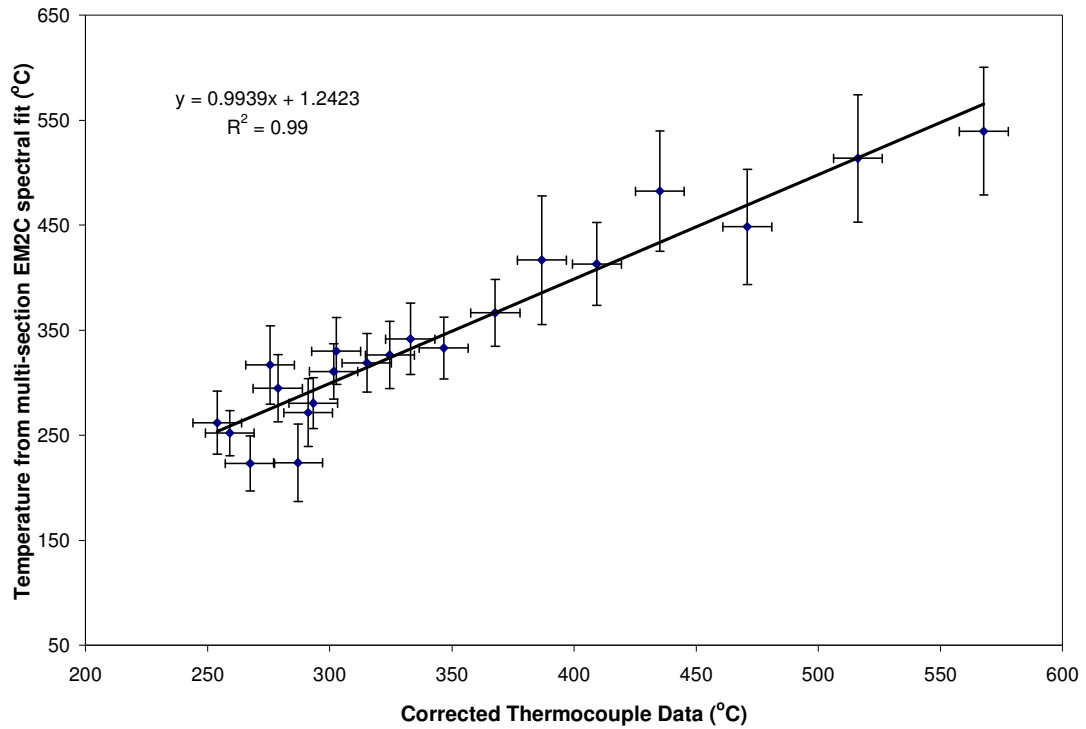
Figure 5-15: Corrected thermocouple data vs. temperature from multi-section EM2C fit
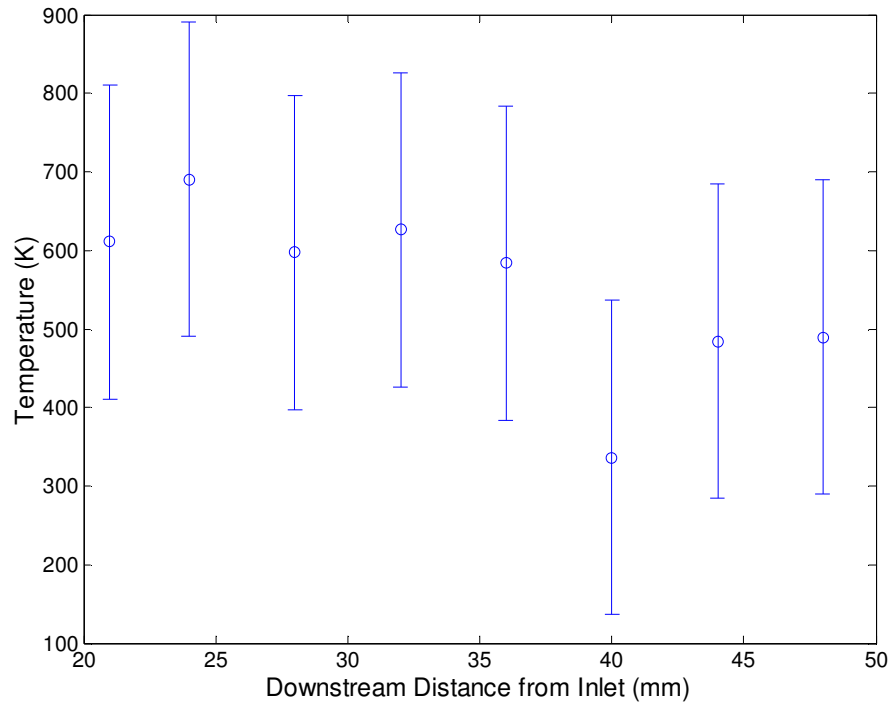
Figure 5-16: Gas temperature near the wall found by fit using discretization of the path versus downstream distance from the inlet: ϕ = 0.86, U=44 cm/s, 2.15 mm wafer spacing

5.4 – Determining Wall Temperature Using an IR Camera

In order to find the surface temperature of the silicon wafers, a ThermaCam SC3000 IR camera from FLIR systems was employed to measure the temperature distribution across the wafer surface. Figure 5-17 shows the relationship between the IR camera and the burner. Figure 5-18 shows the raw infrared image returned by the infrared camera. While the emmisivity of silicon is not constant with increasing temperature, the software used to interpret the image (ThermaCAM Researcher 2002) assumes a constant emissivity for the entire image.
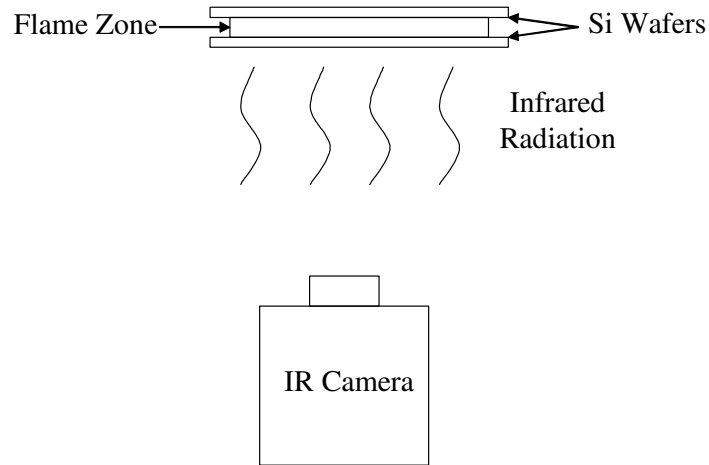
Figure 5-17: Schematic of IR camera setup

As a result, it was necessary to 'reverse engineer' the temperature interpretation process in order to obtain a correct measure of the axial temperature distribution along the silicon wafer's surface. The thermal radiation to the camera based on a constant value for the emissivity is:

$$\dot{q} = \sigma \varepsilon T^4 \tag{20}$$

where σ is the Stefan-Boltzmann constant, ε is the emissivity and T is the temperature of the silicon surface. By using a thermocouple to probe several points in the on the wafer, Equation 20 was used to infer the emissivity of the wafer as a function of temperature. This, in turn, was used to correct the temperatures predicted by the camera for the effect of non-uniform emissivity.
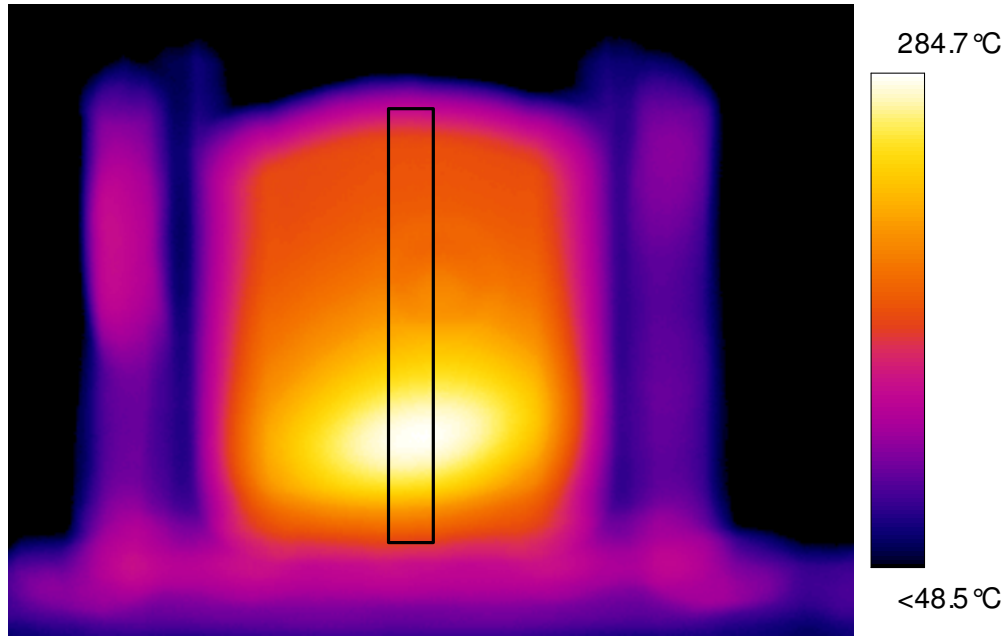
Figure 5-18: IR image of combustor with the interrogation region of the FTIR beam shown by the black box: $\phi = 0.86$, U = 44 cm/s, 2.15 mm wafer spacing, $\varepsilon = 0.6$

Figure 5-19 compares the wafer surface temperatures measured using the corrected IR camera data to the near-wall gas temperatures measured using the spectroscopic technique for the CH_4-air flame with $\phi = 0.82$, U = 44 cm/s and wafer spacing of 2.15 mm. It shows that the near wall gas temperature and the silicon surface temperature are close to each other but, as expected, the near wall gas temperature is slightly higher than the wall temperature. Figure 5-20 compares all of the axial temperature measurements made in the burner.
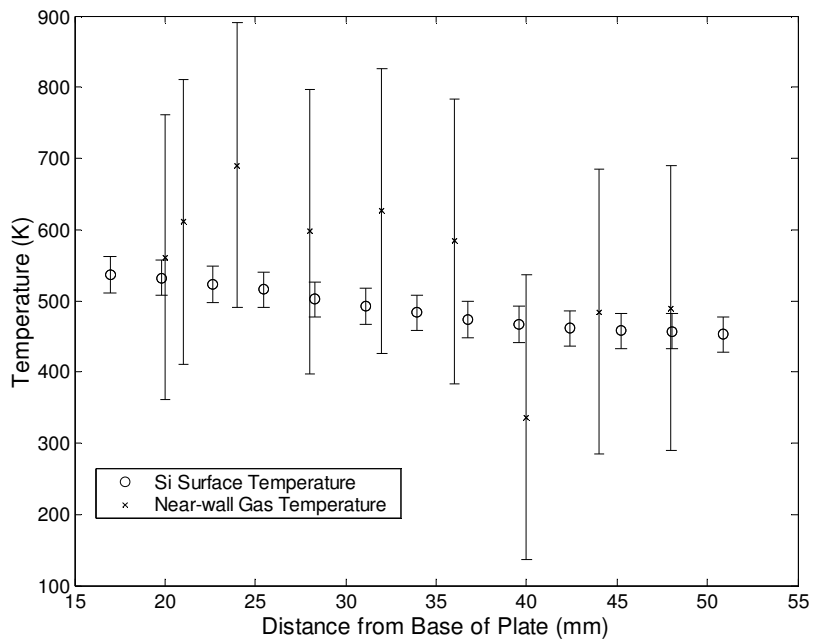
Figure 5-19: Surface temperature profile of the centerline of the silicon wafer and near-wall gas temperature found using discretized fit for 2.15 mm wafer spacing, ϕ = 0.86, and U = 44 cm/s
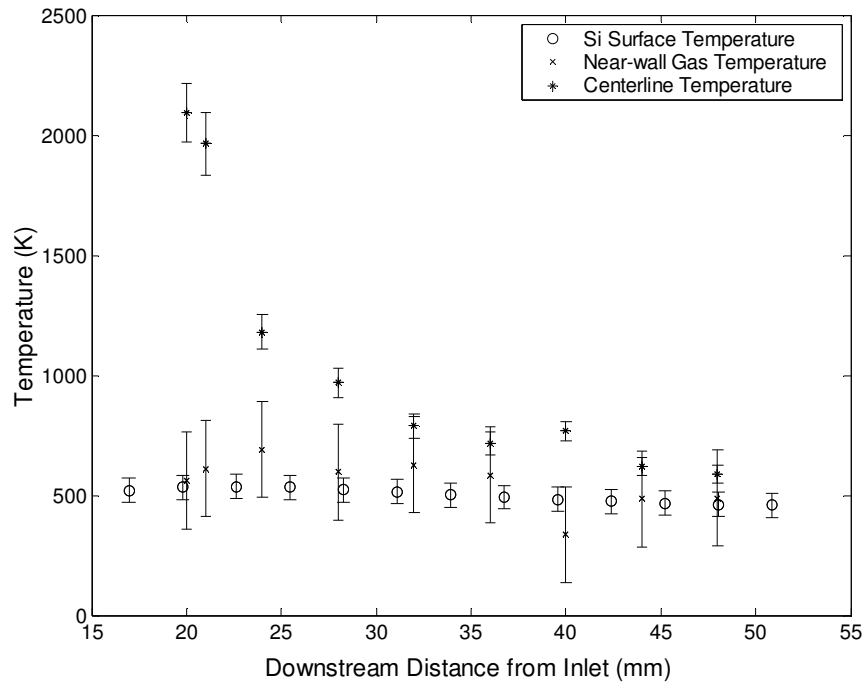
Figure 5-20: Centerline, near wall gas, and silicon surface temperature: ϕ = 0.86, U = 44 cm/s, 2.15 mm wafer spaceing

5.5 - Simple Check of Temperature Measurements

A further check of the accuracy of the temperature measurements is to perform an overall energy balance on the combustor.

$$\dot{Q}_R = \dot{Q}_{loss} + \dot{Q}_{ext} \tag{21}$$

In this expression, $\dot{Q}_R$ is the heat release rate from the combustion of the fuel, $\dot{Q}_{loss}$ is the heat transfer rate to the combustor walls, and $\dot{Q}_{ext}$ is the enthalpy convected out by the flow through the combustor exit (or exhausted to the environment).

The heat loss to the walls is computed assuming that the Nusselt number is 7.54, the value for a fully developed flow between two infinite parallel plates of constant temperature [49]. The expression for the heat transfer rate at a particular axial position in the flame is:

$$\dot{q} = \frac{Nu \cdot k}{d_{gap}}(T_{cl} - T_w) \tag{22}$$

where k is the thermal conductivity of air, d_{gap} is the plate spacing, T_{cl} and T_w are the respectively the centerline gas and wall temperatures. The net heat transfer from the gas to the walls of the burner is calculated by substituting Equation 21 in Equation 22 where the centerline gas temperature comes from the profile shown in Figure 5-12 and the wall temperature comes from thermocouple measurements.

$$\dot{Q}_{wall} = \int \dot{q}W\Delta z dy \tag{23}$$

In Equation 23, Δz is the distance between measurement points, W is the width of the combustor and $\dot{q}$ is the heat transfer calculated at that point. Using a value for k of

70×10^{-3} (W/(m-K)) corresponding to air at 1000 K and a 2.15 mm gap, the estimated value for the heat transfer to the wall is approximately 275 W.

The heat release rate $\dot{Q}_R$ is calculated using:

$$\dot{Q}_R = \dot{m}H_{Rx} \tag{24}$$

where $\dot{m}$ is the mass flow rate of fuel, and H_{Rx} is the heat of reaction determined using Gaseq [50]. This turns out to be 17.6 MJ/kg for this CH_4-air flame at f = 0.86. Thus, the overall heat release rate due to chemical reaction is estimated to be 650 W based on the combustor dimensions of 2.15 mm x 6 cm long and U = 44 cm/s.

The heat exhausted out the end of the combustor can be estimated by:

$$\dot{Q}_{ext} = \int \rho u c_p T(y) \Delta y \, dy \tag{25}$$

where ρ is the density of the gas, u is the flow speed, c_p is the heat capacity, T(y) is the temperature of the discrete section, and Δy is the width of the discrete section. Assuming that the exhaust gas is very close in composition to air and has constant properties at 550 K since there is a very low temperature gradient at the end of the combustor (~100 K), the heat exhausted to the environment is estimated to be 350 W. Putting it all together, the sum of the heat of the exhaust and heat loss to the walls is 625W which is very close to the estimate of 650 W for the heat of combustion. Given the simplicity of the heat flux estimates and the fact that radiation to the environment was not included, we can conclude that the temperature measurements are self-consistent and that the wall heat fluxes predicted based on the parabolic gas temperature profiles are not unrealistic. Table 1 summarizes the values of the parameters used in the calculation of heat fluxes.

Table 2: Parameters used in heat flux calculation

Parameter	Value	Units	Reference
c_p	1.039	kJ/(kg-K)	air (T = 550 K) [48]
k_{gas}	0.0426	W/(m-K)	air (T = 550 K) [48]
ρ	0.642	kg/m^3	air (T = 550 K) [48]
H_{Rx}	17.6	MJ/kg	[50]
N_u	7.54		
W	60	mm	
d_{gap}	2.15	mm	
u	44	cm/s	

5.6 – Concentration Measurements

Concentration as a function of downstream distance was found using the methods discussed in chapter 3 for various conditions. Figure 5-21 shows concentrations of CO_2 and CH_4 versus downstream distance from the inlet. The wafer spacing is 2.15 mm, $\phi = 0.82$ and U = 44 cm/s. Due to the interference from the silicon wafer on the CO_2 band, the CO_2 concentration measurements show more scatter and have larger error bars than the CH_4 concentration measurements, which are not affected by the interference. The calculations for the error bars for concentration in Figure 5-21 are reviewed in Appendix C.
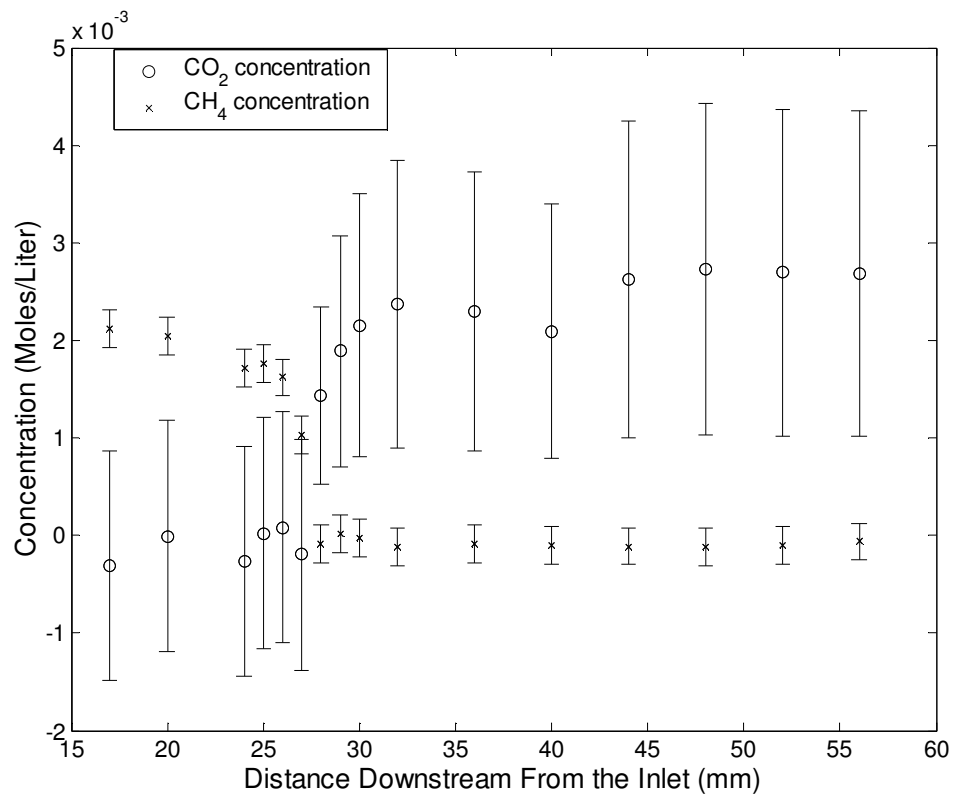
Figure 5-21: CO_2 and CH_4 concentrations vs. downstream distance from the inlet: The reactants are CH_4 and air with $\phi = 0.82$ U = 44 cm/s

Chapter 6 – Conclusion

This work describes the development and deployment of infrared diagnostic techniques suitable for making measurements of species concentration and gas temperature in micro-combustors. The centerline gas temperature, wall gas temperature and the concentrations of reactants and products were measured at different downstream distances in a silicon-walled micro-burner developed to simulate a 'real' MEMS device.

Species concentrations are determined using the area under the band for CO_2 and the peak of the Q branch for CH_4. The temperature of the gas is found by fitting a spectral band model for CO_2 absorbance to CO_2 spectra measured in the micro-burner.

These two types of measurements will enable one to determine the chemical and overall efficiency of a micro-combustor. This technique, if improved, is expected to be useful for developers of silicon-MEMS based micro-combustors because the measurements were made in-situ by imaging through silicon walls which are transparent in the infrared.. Since the spatial resolution could not be made lower than 1 mm, the flame thickness could not be measured accurately.

The results show that silicon is not the ideal wall material for micro-combustors. Its high thermal conductivity leads to large thermal losses and the material is a problematic optical window for this application because of its dramatic loss of transmittance at temperatures higher than $400^{o}C$. Nevertheless, this work has shown that measurements of species concentration and temperature are possible. For reactions where the wall temperatures remain below $400^{o}C$, this technique holds a lot

of promise. Finally, this diagnostic might be especially well suited for micro-

combustors that utilize catalytic reactions since these could potentially operate at

much lower temperatures where silicon absorbance is less significant.

Chapter 7 - Future Work

7.1 - Limitations to Be Addressed

While capable of measuring temperature and concentration well, this technique has several shortcomings that need to be addressed in order for it to be used on a wider scale and in more applications. The first involves signal strength and path length which must be addressed together because they both contribute to the final signal to noise ratio. Since absorbance is proportional to the concentration and path length, the short path length results in a small absorbance, and when coupled with the low signal strength, results in a low signal to noise ratio, limiting the range of measurements that can be made.

To increase the signal strength, different silicon plates could be used. Single side polished plates with a lower roughness on the unpolished side would increase the transmittance. The signal strength could also be boosted by increasing the intensity of the source. Another but more challenging way to increase the signal strength would be to use two double polished plates. The challenge would be to eliminate the effects of etaloning by correcting the background and sample scans with a function describing the interference. This could be difficult because the interference pattern from the etaloning would have to be modeled very accurately and the wafer spacing, angle of the burner with respect to the beam, reflectivity of the wafers, and coefficient of thermal expansion may have to be known with a high degree of precision.

The spatial resolution is another factor limiting the signal strength. In order to achieve the required 1 mm spatial resolution, a mask used which 'throws away' a significant portion of the initial energy. A better approach would be to eliminate the mask and collimate the beam to achieve the desired spatial resolution. This will be difficult because of the nature of the source, which is a relatively large heated filament with a low spatial coherence. Boosting the intensity of the source and using a very small aperture might help to make the beam more spatially coherent and easier to collimate in a small beam diameter. With this method it might be possible to reduce the spatial resolution to 0.25 mm or less.

Another factor affecting the signal strength is the transmittance of the silicon wafers. Since the transmittance drops with temperature for silicon, it may be possible to use a different material for optical access when the walls are hotter than 300°C. An optical material like sapphire would be good because it has better temperature stability than silicon and it would result in much greater light throughput. The drawback is that the MEMS applications would be much more limited because of the difficulties associated with integrating the sapphire window into the manufacturing process.

The path length could be lengthened by looking along the path parallel to the wafers instead of perpendicular to them. This would increase the absorbance thereby increasing the signal to noise ratio. This would allow low concentration species such as CO to be measured and the overall combustion efficiency to be determined. One could also probe the rotational structure of CO to get temperature. To realize a

longer path length, however, the beam divergence must also be reduced so that a spatial resolution below 1 mm is maintained for the entire length of the path.

7.2 - Extensions to This Work

This diagnostic technique could be extended in several ways for new measurements. First, coupling the beam to an optical fiber would make it simple to apply the technique to different experiments. A small parabolic mirror could be built to fit on the end of the fiber to collimate the emerging beam through the combustor while another mirror and fiber at the other end could capture the light as it exits. Any combustor made of a material that is optically transparent in the infrared could be investigated. Coupling the beam to a fiber would be useful especially where a large optical assembly is not practical and a compact system is more desirable.

Second, this technique could be applied to images of absorbance at different wavelengths. (hyperspectral imaging) This would enable one to find the values of concentration and temperature simultaneously over the entire imaging area. The step-scan feature of the Nexus 870 FTIR spectrometer used in the experiment may make this possible by allowing the moving mirror to pause in a particular location. A photo-array (IR camera) would acquire an image of the absorbance. Once a complete set of images spanning the spectral range has been obtained, the change in intensity at each pixel as a function of frame number (analagous to wavelength) could be used to determine CO_2 concentration and temperature simultaneously. CH_4 concentration could also be determined if a different spectral region was chosen.

Finally, a method for measuring temperature based on methane spectra could be made possible by building a narrow band model for methane. Such a fuel-based

model could be used to measure the temperature before the flame. When combined

with CO_2 based post flame measurements, one could generate an overall temperature

profile through the flame which could be used to determine flame thickness.

Appendix A – Fortran code implementing EM2C model

```
C*******************************************************************
      ***
C
C     CALCULATION OF RADIATIVE INTENSITY AND TRANSMISSIVITY OF
C      A NONISOTHERMAL AND NONHOMOGENEOUS MIXTURE COLUMN OF H2O-
CO2-CO-
C     TRANSPARENT GAS-PARTICLES DISCRETIZED INTO N HOMOGENEOUS AND
C      ISOTHERMAL ELEMENTS
C
C     WITH THE MALKMUS STATISTICAL NARROW-BAND MODEL AND
C     THE CURTIS-GODSON APPROXIMATION AND A 25 cm-1 SPECTRAL
RESOLUTION
C
C     THE INPUTS (FILE 'SNBINPUT') :
C     ***************************
C
C      - N : TOTAL NUMBER OF ELEMENTS
C      - FOR I VARYING FROM 1 TO N :
C       LENGTH(CM),TEMPERATURE(K),PRESSURE(ATM),XH2O,XCO2,XCO,XSOOT
C       (XSPEC = MOLAR FRACTION OF SPECIES SPEC=H2O,CO2 or CO)
C       (XSOOT = VOLUME FRACTION OF PARTICLES IN THE MIXTURE)
C        (EACH LINE CORRESPONDS TO ONE ELEMENT I)
C       (THE DIRECTION OF PROPAGATION IS FROM N TO 1)
C
C     THE OUTPUTS ARE :
C     ****************
C
C     FILE 'SNBINTENS' :
C     ------------
C
C      - WAVE NUMBER (CM-1), SPECTRAL RADIATIVE INTENSITY AT
C        THE EXIT OF THE COLUMN  (IN W.M-2.STR-1.(CM-1)-1)
C      - TOTAL RADIATIVE INTENSITY (IN W.M-2.STR-1)
C
C     FILE 'SNBTRANS' :
C     -------------
C
C      - WAVE NUMBER (CM-1), TRANSMISSIVITY
C
C     THE OTHER FILES REQUIRED FOR THIS PROGRAM ARE :
C     ***********************************************
C
C      - SNBWN : CONTAINS THE WAVE NUMBERS FOR WHICH CALCULATIONS ARE
C        CARRIED OUT AND SPECTRAL WIDTHS BOTH IN cm-1
C          THE PROGRAM IS STOPPED WHEN A NEGATIVE WAVE NUMBER IS
C          ENCOUNTERED
C          THE WAVE NUMBERS MUST BE WITHIN THE RANGE 150-9300 cm-1
C
C      - SNBH2O : H2O SNB PARAMETERS
C      - SNBCO2 : CO2 SNB PARAMETERS
C      - SNBCO  : CO  SNB PARAMETERS
```

```
C****************************************************************
***
      IMPLICIT DOUBLE PRECISION (A-C,E-H,O-Z)
      LOGICAL LICO,LICO2,LIH2O
      REAL KCO,KC,KH
      REAL *8 DWVNB
      PARAMETER (NMAX=100,NWVMAX=450)
      COMMON/PHYS/XD(NMAX),T(NMAX),P(NMAX),XH2O(NMAX),XCO2(NMAX),
     .           XCO(NMAX),XSUT(NMAX),N
      COMMON/TAUCOL/TAUIN(NMAX+1)
      COMMON /PLANK/C1,C2
      COMMON /RSPC/WVNB,DWVNB
      COMMON /LINDX/LICO,LICO2,LIH2O
      COMMON /INDEX/ICO,ICO2,IH2O
      COMMON /SPCD/DCO(14,48),DC(14,367),DH(14,367)
      COMMON /SPCK/KCO(14,48),KC(14,367),KH(14,367)
      COMMON /CFSUT/WV55
      COMMON /VALPI/PI
      DIMENSION XLUM(NMAX),XL(NWVMAX),XLS(NWVMAX),WV(NWVMAX)
C
C     READING THE COLUMN DATA FILE
C
      OPEN(UNIT=10,FILE='SNBINTENS')
      OPEN(UNIT=11,FILE='SNBTRANS')
      OPEN(UNIT=8,FILE='SNBINPUT')
      READ(8,*) N
      DO 1 I=1,N
      READ(8,*) XD(I),T(I),P(I),XH2O(I),XCO2(I),XCO(I),XSUT(I)
1     CONTINUE
      X=1.
      PI=4.0*DATAN(X)
C
C     READING THE MODEL PARAMETERS
C
      CALL PARAM
      MF=1
      NF=1
C
C     WAVE NUMBER LOOP
C
      IWVNB=0
      OPEN(UNIT=9,FILE='SNBWN')
1000  CONTINUE
      IWVNB=IWVNB+1
      READ(9,*) WVNB,DWVNB
      IF(WVNB.LT.0.) GOTO 1001
      WV55=WVNB*5.5
      WV(IWVNB)=WVNB
C
C     CALCULATION OF THE SPECTRAL INDEX FOR EACH SPECIES
C
      CALL FINDI
C
C     CALCULATION OF BLACKBODY INTENSITIES
C
      DO 3 I=1,N
      TT=T(I)
```

```
        XLUM(I)=XLU(TT)
3       CONTINUE
C
C       CALCULTATION OF TRANSMISSIVITIES
C
        CALL TRSMI
C
C       CALCULATION OF RADIATIVE INTENSITIES
C
        XL(IWVNB)=0.
        DO 4 I=1,N
        XL(IWVNB)=XL(IWVNB)+XLUM(I)*(TAUIN(I)-TAUIN(I+1))
4       CONTINUE
        XLS(IWVNB)=XL(IWVNB)/DWVNB
        WRITE(11,*) WVNB, TAUIN(N+1)
        WRITE(10,*) WVNB,XLS(IWVNB)
        GOTO 1000
1001    CONTINUE
        NWV=IWVNB-1
        XLT=0.
        DO 5 J=1,NWV
        XLT=XLT+XL(J)
5       CONTINUE
        WRITE(10,*) XLT
        REWIND(UNIT=9)
        CLOSE(UNIT=10)
        CLOSE(UNIT=11)
        CLOSE(UNIT=8)
        STOP
        END
C
C****************************************************************
C                                                              *
C       BLACKBODY INTENSITY (PLANCK FORMULA)                   *
C                                                              *
C****************************************************************
C
        DOUBLE PRECISION FUNCTION XLU(T)
        IMPLICIT DOUBLE PRECISION (A-H,O-Z)
        COMMON /PLANK/C1,C2
        COMMON /VALPI/PI
        C2T=C2/T
        C2T=DEXP(C2T)-1.0
        XLU=C1/C2T
        RETURN
        END
C
C
C****************************************************************
C                                                              *
C    THIS SUBROUTINE READS THE MODEL PARAMETERS                *
C                                                              *
C****************************************************************
C
        SUBROUTINE PARAM
        REAL KCO,KC,KH
        COMMON /SPCD/DCO(14,48),DC(14,367),DH(14,367)
```

```fortran
      COMMON /SPCK/KCO(14,48),KC(14,367),KH(14,367)
      OPEN(UNIT=45,FILE='SNBCO')
      OPEN(UNIT=46,FILE='SNBCO2')
      OPEN(UNIT=47,FILE='SNBH2O')
C
C   READING THE PARAMETERS
C
      DO 1 I=1,48
1     READ(45,*) (KCO(J,I),J=1,12)
      DO 2 I=1,48
2     READ(45,*) (DCO(J,I),J=1,12)
      DO 3 I=1,96
3     READ(46,*) (KC(J,I),J=1,14)
      DO 4 I=1,96
4     READ(46,*) (DC(J,I),J=1,14)
      DO 5 I=1,367
5     READ(47,*) (KH(J,I),J=1,14)
      DO 6 I=1,367
6     READ(47,*) (DH(J,I),J=1,14)
      RETURN
      END
C
C
C*******************************************************************
****
C
*
C      THIS SUBROUTINE CALCULATES THE INTERPOLATION COEFFICIENTS
*
C
*
C*******************************************************************
****
C
      SUBROUTINE TMNO(TM,RT,IT)
      DOUBLE PRECISION TM,RT
      IF(TM.GT.300.0) THEN
         IF(TM.LT.2900.0) THEN
            RT=(TM-300.0)/200.0
            IT=INT(RT+1.0E-6)
            RT=RT-IT
            IT=IT+1
         ELSE
            RT=1.0
            IT=11
         ENDIF
      ELSE
         RT=0.0
         IT=1
      ENDIF
      RETURN
      END
C
C
C*******************************************************************
C                                                                 *
C      THIS SUBROUTINE SEARCHS THE PARAMETER INDEXES              *
```

```
C      CORRESPONDING THE WAVE NUMBER 'WVNB'                      *
C                                                               *
C****************************************************************
C
       SUBROUTINE FINDI
       IMPLICIT DOUBLE PRECISION (A-H,O-Z)
       LOGICAL LICO,LICO2,LIH2O
       COMMON /LINDX/LICO,LICO2,LIH2O
       COMMON /INDEX/ICO,ICO2,IH2O
       COMMON /PLANK/C1,C2
       COMMON /RSPC/WVNB,DWVNB
C
C   CALCULATION OF PLANCK LAW PARAMETERS
C
       C1=(0.11909E-7)*WVNB**3*DWVNB
       C2=1.4388*WVNB
C
C   LOOKING FOR THE INDEXES
C
       IF(WVNB.LT.450.0.OR.WVNB.GT.1200) GO TO 10
       ICO2=INT((WVNB-450.)/25.)+1
       GO TO 14
10     IF(WVNB.LT.1950.0.OR.WVNB.GT.2450.) GO TO 11
       ICO2=INT((WVNB-1950.)/25.)+32
       GO TO 14
11     IF(WVNB.LT.3300.0.OR.WVNB.GT.3800.) GO TO 12
       ICO2=INT((WVNB-3300.)/25.)+53
       GO TO 14
12     IF(WVNB.LT.4700.0.OR.WVNB.GT.5250.) GO TO 13
       ICO2=INT((WVNB-4700.)/25.)+74
       GO TO 14
13     ICO2=-9
14     CONTINUE
       IF(WVNB.GE.150.AND.WVNB.LE.9300.) THEN
         IH2O=INT((WVNB-150.)/25.)+1
       ELSE
         IH2O=-9
       ENDIF
       IF(WVNB.LT.1750.0.OR.WVNB.GT.2325.) GO TO 19
       ICO=INT((WVNB-1750.)/25.)+1
       GO TO 21
19     IF(WVNB.LT.3775.0.OR.WVNB.GT.4350.) GO TO 20
       ICO=INT((WVNB-3775.)/25.)+25
       GO TO 21
20     ICO=-9
21     CONTINUE
       LICO=ICO.GT.0
       LICO2=ICO2.GT.0
       LIH2O=IH2O.GT.0
       RETURN
       END
C
C
C************************************************************
C                                                          *
C      CALCULATION OF THE TRANSMISSIVITY OF A INHOMOGENEOUS *
C      COLUMN WITH CURTIS-GODSON APPROXIMATION              *
```

```
C      TRANSMISSIVITIES ARE CALCULATED BETWEEN THE FIRST     *
C      POINT AND A CURRENT POINT OF THE COLUMN               *
C                                                            *
C*************************************************************
C
C
       SUBROUTINE TRSMI
       IMPLICIT DOUBLE PRECISION (A-C,E-H,O-Z)
       REAL KCO,KC,KH
       LOGICAL LICO,LICO2,LIH2O
       PARAMETER (NMAX=100)
       COMMON/PHYS/XD(NMAX),T(NMAX),P(NMAX),XH2O(NMAX),XCO2(NMAX),
      .           XCO(NMAX),XSUT(NMAX),N
       COMMON /LINDX/LICO,LICO2,LIH2O
       COMMON /SPCD/DCO(14,48),DC(14,367),DH(14,367)
       COMMON /SPCK/KCO(14,48),KC(14,367),KH(14,367)
       COMMON /INDEX/ICO,ICO2,IH2O
       COMMON /CFSUT/WV55
       COMMON/TAUCOL/TAUIN(NMAX+1)
       DIMENSION XKCO(NMAX),XDCO(NMAX),XBCO(NMAX)
       DIMENSION XKCO2(NMAX),XDCO2(NMAX),XBCO2(NMAX)
       DIMENSION XKH2O(NMAX),XDH2O(NMAX),XBH2O(NMAX)
       DIMENSION RRT(NMAX),IIT(NMAX),XH(NMAX)

       NCOL=N+1
       DO 1 J=1,NCOL-1
       XH(J)=XD(J)
       CALL TMNO(T(J),RT,IT)
       RRT(J)=RT
       IIT(J)=IT
       T296=296./T(J)
       T273=273./T(J)
       T900=900./T(J)
       XN2=1.-XCO(J)-XCO2(J)-XH2O(J)
       IF(LICO) THEN
         GAM=0.07*XCO2(J)+0.06*(XCO(J)+XN2+XH2O(J))
         GAM=P(J)*GAM*SQRT(T273)
         XKCO(J)=KCO(IT,ICO)+RT*(KCO(IT+1,ICO)-KCO(IT,ICO))
         XDCO(J)=DCO(IT,ICO)+RT*(DCO(IT+1,ICO)-DCO(IT,ICO))
         XBCO(J)=2.*GAM*XDCO(J)
       ENDIF
       IF(LICO2) THEN
         GAM=0.07*XCO2(J)+0.058*XN2+0.15*XH2O(J)
         IF(T(J).LE.900.) THEN
         GAM=P(J)*GAM*(T296)**0.7
         ELSE
         GAM=P(J)*GAM*0.45913*DSQRT(T900)
         ENDIF
         XKCO2(J)=KC(IT,ICO2)+RT*(KC(IT+1,ICO2)-KC(IT,ICO2))
         XDCO2(J)=DC(IT,ICO2)+RT*(DC(IT+1,ICO2)-DC(IT,ICO2))
         XBCO2(J)=2.*GAM*XDCO2(J)
       ENDIF
       IF(LIH2O) THEN
         RATT=DSQRT(T296)

GAM=0.066*(7.0*RATT*XH2O(J)+1.2*(XH2O(J)+XN2)+1.5*XCO2(J))*RATT
         GAM=P(J)*GAM
```

```
        XKH2O(J)=KH(IT,IH2O)+RT*(KH(IT+1,IH2O)-KH(IT,IH2O))
        XDH2O(J)=DH(IT,IH2O)+RT*(DH(IT+1,IH2O)-DH(IT,IH2O))
        XBH2O(J)=2.*GAM*XDH2O(J)
        ENDIF
1       CONTINUE
C
C       THE TRANSMISSIVITIES ARE INITIALIZED WITH THE TRANSMISSIVITY
C       OF THE PARTICLES.
C
        TAUIN(1)=1.
        DO 12 I=1,NCOL-1
        HSUIE=0.
        DO 12 J=2,NCOL
        HSUIE=HSUIE-XH(J-1)*WV55*XSUT(J-1)
        TAUIN(J)=DEXP(HSUIE)
12      CONTINUE
        XMCO=0.
        XMCO2=0.
        XMH2O=0.
        DO 4 I=1,NCOL-1
        HT=HT+XH(I)
        XMCO=XMCO+XCO(I)
        XMCO2=XMCO2+XCO2(I)
        XMH2O=XMH2O+XH2O(I)
4       CONTINUE
C
C       CALCULATION OF CO TRANSMISSIVITY
C
        IF(LICO.AND.XMCO.GT.1.0E-6) THEN
        SC=0.
        SK=0.
        SB=0.
        DO 3 J=2,NCOL
        YC=XCO(J-1)*P(J-1)*XH(J-1)
        YK=YC*XKCO(J-1)
        YB=YK*XBCO(J-1)
        SC=SC+YC
        IF(SC.GT.1.D-12) THEN
        SK=SK+YK
        SB=SB+YB
        ZC=SC
        ZK=SK/ZC
        ZB=SB/SK
        XK=1.0+2.0*ZK*ZC/ZB
        TAUIN(J)=TAUIN(J)*DEXP(-ZB*(DSQRT(XK)-1.0))
        ENDIF
3       CONTINUE
        ENDIF
C
C       CALCULATION OF CO2 TRANSMISSIVITY
C
        IF(LICO2.AND.XMCO2.GT.1.0E-6) THEN
        SC=0.
        SK=0.
        SB=0.
        DO 5 J=2,NCOL
        YC=XCO2(J-1)*P(J-1)*XH(J-1)
```

```fortran
      YK=YC*XKCO2(J-1)
      YB=YK*XBCO2(J-1)
      SC=SC+YC
      IF(SC.GT.1.D-12.AND.YK.GT.1.D-15) THEN
      SK=SK+YK
      SB=SB+YB
      ZC=SC
      ZK=SK/ZC
      ZB=SB/SK
      XK=1.0+2.0*ZK*ZC/ZB
      TAUIN(J)=TAUIN(J)*DEXP(-ZB*(DSQRT(XK)-1.0))
      ENDIF
5     CONTINUE
      ENDIF
C
C     CALCULATION OF H2O TRANSMISSIVITY
C
      IF(LIH2O.AND.XMH2O.GT.1.0E-6) THEN
      SC=0.
      SK=0.
      SB=0.
      DO 6 J=2,NCOL
      YC=XH2O(J-1)*P(J-1)*XH(J-1)
      YK=YC*XKH2O(J-1)
      YB=YK*XBH2O(J-1)
      SC=SC+YC
      IF(SC.GT.1.D-12) THEN
      SK=SK+YK
      SB=SB+YB
      ZC=SC
      ZK=SK/ZC
      ZB=SB/SK
      XK=1.0+2.0*ZK*ZC/ZB
      TAUIN(J)=TAUIN(J)*DEXP(-ZB*(DSQRT(XK)-1.0))
      ENDIF
6     CONTINUE
      ENDIF
      RETURN
      END
```

Appendix B - Least square curve fitting routine utilizing EM2C code

```
% Script to find peak temperature by using multiple paths based on parabolic
temperature
% profile for EM2C.

clear all
close all
% Add path for band functions
addpath('C:\Work\CDEM Lab\Micro-Combustor\Band Models')

% load in the spectra
spectra = load('C:\Work\CDEM Lab\Micro-
Combustor\Data\17June04\run2\z_20mm.CSV');

nu_s = spectra(:,1);
abs_s = spectra(:,2);

% Find rms noise in spectra
% Search in area of band with no interference from molecules
index(1) = Locate(nu_s,2500,20);
index(2) = Locate(nu_s,2700,20);

abs_rms = abs_s(index(1):index(2),:);

rms_noise = std(abs_rms);

% Do search for area of interest
% Locate uses a binary search to find the point closest but still <= the value specified
index(1) = Locate(nu_s,2000,20);
index(2) = Locate(nu_s,2500,index(1)+100);

nu = nu_s(index(1):index(2));
abs_band = abs_s(index(1):index(2));

% Do a baseline correction on the experimental data.
% Do a polynomial least squares fit using the end of the band 2050-2100 and 2450-
2550
[n,m] = size(nu);
ind(1) = Locate(nu,2100,5);
ind(2) = Locate(nu,2450,5);
% [P, S] = polyfit(nu(1:ind(1)),abs(1:ind(1)),1);
[P, S] =
polyfit([nu(1:ind(1));nu(ind(2):n)],[abs_band(1:ind(1));abs_band(ind(2):n)],2);
```

```
corr = P(1)*nu.^2 + P(2)*nu + P(3);
abs_corr = abs_band - corr;

% Call curve fitting function
% Initialize variables for function
PL = 0.215;     % Pathlength in cm
XH2O = 0;     % Molar fraction of water
XCO = 0;      % Molar fraction of water
P = 1;        % Pressure in atm

% Locate 2300cm-1 and 2150 cm-1
ind(3) = Locate(nu,2300,5);
ind(4) = Locate(nu,2150,5);
nu_fit = nu(ind(4):ind(3));
abs_fit = abs_corr(ind(4):ind(3));

% Setup parabolic temperature profile of T = a*x^2+b*x+c
% Since c = Twall then 'b' is a function of 'a'
% b = -a*x_width
% Variable X = [a, XCO2]
% The path is split in n parts: n should be odd!
n_pl = 15;

% Guess values for a, b and XCO2
X0 = [-10000, 200, 0.02];
% Lower and Upper bounds
lb = [-2000000, 0, 0.000001];
ub = [2000000, 1000, 100];
options = optimset('TolFun',1e-10, 'LargeScale','on');

[X, resnorm, residual] = lsqcurvefit(@em2c_multipath, X0, nu_fit, abs_fit, lb, ub,
options, PL, P, XH2O, XCO, n_pl);

% call model to get values for comparison plot
abs_model = em2c_multipath(X, nu_fit, PL, P, XH2O, XCO, n_pl);
residual2 = abs_fit - abs_model;

sse = sum(residual2.^2);
sst = sum(abs_fit.^2) - sum(abs_fit).^2/(2*n+1);
X

rsq = 1- sse/sst

dT = 1;
abs_model2 = em2c_multipath([X(1)+dT,X(2),X(3)], nu_fit, PL, P, XH2O, XCO,
n_pl);
```

```
abs_model3 = em2c_multipath([X(1),X(2)+dT,X(3)], nu_fit, PL, P, XH2O, XCO,
n_pl);
dA = sqrt(sum(abs(abs_model2 -abs_model))^2 + sum(abs(abs_model3 -
abs_model))^2);
% Find dT_peak
T_peak_1 = (X(1)+dT)*(PL/2)^2-(X(1)+dT)*PL^2/2 + X(2);
T_peak_2 = X(1)*(PL/2)^2-X(1)*PL^2/2 + X(2)+dT;
T_peak = X(1)*(PL/2)^2-X(1)*PL^2/2 + X(2)
delta_T = sqrt((T_peak_1-T_peak)^2 + (T_peak_2-T_peak)^2);
dF_da = delta_T/dA;
error_T = dF_da*sqrt(abs(sum(abs(residual))^2-(length(nu_fit)*rms_noise)^2))

rmpath('C:\Work\CDEM Lab\Micro-Combustor\Band Models')
```

Function EM2C called in least squares curve fitting routine:

```
function abs = em2c_mulitpath(X, nu_exp, PL, P, XH2O, XCO, n)
% Function to run band model EM2C for a given set of inputs
% including multiple paths to fit to a parabolic temperature profile
%
% PL in cm, Temperature T in K, Pressure P in atm
% XCO2, XH2O, XCO in molar fraction

% Save working directory and change to band model directory
curr_dir = pwd;
cd('c:\Work\CDEM Lab\Micro-Combustor\Band Models')

a = X(1);
XCO2 = X(3);
c = X(2);

b = -a*PL;

% Create the input file
% This function looks at a single path and not multiple different paths
fid = fopen('SNBINPUT','w');
% First Line: Number of paths (5 for this function)
fprintf(fid,'%2f\n', n);

% We assume no soot in this problem
XSoot = 0;

% paths
% first path
y = 0;
T = c;
pl_temp =  PL/(n-1);
PL_n = PL/n;
fprintf(fid,'%8.6f %20.15f %3.2f %4.3f %20.18f %4.3f %4.3f \n', PL_n, T, P, XH2O,
XCO2, XCO, XSoot);

for i = 1:(n-1)
   y = i*pl_temp;
   T = a*y^2+b*y+c;
   fprintf(fid,'%8.6f %20.15f %3.2f %4.3f %20.18f %4.3f %4.3f \n', PL_n, T, P,
XH2O, XCO2, XCO, XSoot);
end

status = fclose(fid);
```

```
% Call EM2C
!SNB.exe

% Load the resulting file into a matrix and get nu and tau
load('SNBTRANS')

% change directory back to original
cd(curr_dir)

nu_snb = SNBTRANS(:,1);
tau_snb = SNBTRANS(:,2);

% Use spline fit to and match the spacing of the data points of the experimental data
tau = spline(nu_snb, tau_snb, nu_exp);
abs = log(1./tau);
```

Appendix C – Uncertainty analysis

General Method for Computing Uncertainty

For a given function of *n* variables:

$$y = f(x_1, x_2, ..., x_n) \tag{26}$$

the uncertainty in *y* is [51]:

$$\delta y = \sqrt{\left(\frac{\partial f}{\partial x_1} \delta x_1\right)^2 + \left(\frac{\partial f}{\partial x_2} \delta x_2\right)^2 + ... + \left(\frac{\partial f}{\partial x_n} \delta x_n\right)^2} \tag{27}$$

where δx_i is the uncertainty of the ith variable. When the ith variable represents an average of several measurements, the uncertainty of the ith variable is written as $\delta \bar{x}_i$.

The 95% confidence estimate for $\delta \bar{x}_i$ is [52]:

$$\delta \bar{x}_i = 2\sqrt{\left(\frac{U_i}{2}\right)^2 + \left(S_{\bar{x}_i}\right)^2} \tag{28}$$

where U_i is the 95% confidence interval estimate of the systematic uncertainty in the measurement of $\bar{x}_i$ and $S_{\bar{x}_i}$ is the standard deviation of the mean or the random component of the uncertainty in the measurement of $\bar{x}_i$. This is defined as follows:

$$S_{\bar{x}_i} = \frac{\sigma_{x_i}}{\sqrt{N_j}} \tag{29}$$

where N_j is the number of measurements made of the ith variable to compute the average, and σ_{x_i} is the standard deviation of the measurements of the ith variable.

The standard deviation, in turn, is:

$$\sigma_{x_i} = \left[\frac{1}{N_j - 1} \sum_{j=1}^{N_j} (x_{i,j} - \bar{x}_i)^2 \right]^2 \tag{30}$$

Note that increasing the number of samples N_j reduces the random component of the uncertainty but that the minimum value of the uncertainty is limited by the systematic component U_i.

Taken together, Equations 26 through 30 are used to estimate the uncertainty of all of the measurements reported in this thesis. What follows are descriptions of the specific applications of Equations 26-30 to each type of measurement.

Uncertainty in Calibration Mixture Concentration

Following Equation 26, the function f refers in this case to the mole fraction of CH_4 or CO_2 and air in a particular calibration mixture. This is written as follows:

$$X_{CO_2} = f = \frac{Q_{CO_2}}{Q_{CO_2} + Q_{air}} \tag{31}$$

where Q_{CO_2} is the volumetric flow rate of CO_2 and Q_{air} is the volumetric flow rate of air. The partial derivatives with respect to Q_{CO_2} and Q_{air} corresponding to Equation 27 are:

$$\frac{\partial f}{\partial Q_{CO_2}} = \frac{1}{Q_{CO_2} + Q_{air}} - \frac{Q_{CO_2}}{(Q_{CO_2} + Q_{air})^2} \tag{32}$$

$$\frac{\partial f}{\partial Q_{air}} = - \frac{Q_{CO_2}}{(Q_{CO_2} + Q_{air})^2} \tag{33}$$

Substituting into Equation 27 gives the uncertainty for the concentration of CO_2 in the calibration mixture:

$$\delta X_{CO_2} = \sqrt{\left(\left(\frac{1}{Q_{CO_2}+Q_{air}} - \frac{Q_{CO_2}}{(Q_{CO_2}+Q_{air})^2}\right)\delta Q_{CO_2}\right)^2 + \left(-\frac{Q_{CO_2}}{(Q_{CO_2}+Q_{air})^2}\delta Q_{air}\right)^2} \qquad (34)$$

A similar procedure is used to find the uncertainty in the concentration of CH_4 in the calibration mixture.

Uncertainty in Concentration Determined From Absorption Spectra

As indicated in Section 3.2, the equation used to infer sample concentration from the area under the absorption band is:

$$X = P_1 \overline{A} + P_2 \qquad (35)$$

where X is the unknown mixture mole fraction and $\overline{A}$ is the average area under the absorption spectrum determined from several absorption scans. P_1 and P_2 are respectively the slope and intercept of the linear least-squares fit to the calibration data. Applying Equation 27 to Equation 35 gives the expression for the uncertainty in the unknown mixture mole fraction:

$$\delta X = \sqrt{\left(\overline{A}\,\delta P_1\right)^2 + \left(\delta P_2\right)^2 + \left(P_1\delta\overline{A}\right)^2} \qquad (36)$$

In this work, the output of the spectrometer was an average spectrum computed from 100 individual co-added spectra. The co-added spectra were imported into MATLAB where the functions 'CO2conc' and 'CH4conc' were used to integrate the appropriate region of the co-added spectrum (2100 to 2450 cm^{-1} for CO_2 and 2800 to 3250 cm^{-1} for CH_4) to determine $\overline{A}$. As a result, the variation in the areas corresponding to the individual spectra that make up the co-added spectra are not available and thus the uncertainty in $\overline{A}$ cannot be determined using Equations 27-29. Instead, the RMS variation in absorbance with wavenumber (σ_{rms}) in an area of the

spectrum where no absorbance is expected is used to estimate the uncertainty in $\overline{A}$.

This is the procedure recommended by the manufacturer of the instrument. The

spectral region used to estimate the RMS variation in $\overline{A}$ is from 2500 to 2700 cm^{-1}

and the RMS variation in $\overline{A}$ is $\Delta v \sigma_{rms}$ where Δv is the wavelength interval

corresponding to the interval over which $\overline{A}$ is calculated. So, we assume

$$\delta \overline{A} = \Delta v \sigma_{rms} \tag{37}$$

The values of $\delta \overline{A}$ over the relevant bands are 6.05e-5 cm^{-1} for CO_2 and 1.41e-4 for

CH_4.

The uncertainties of the linear fit parameters P_1 and P_2 can be estimated using

the following expressions from Taylor [45]:

$$\delta P_1^{\,2} = \frac{\sigma_{\overline{A}}^{\,2} (\sum_i \overline{A}_{i,cal}^{\,2})}{N_{cal} (\sum_i \overline{A}_{i,cal}^{\,2}) - (\sum_i \overline{A}_{i,cal})^2} \tag{38}$$

$$\delta P_2^{\,2} = \frac{N_{cal} \sigma_{\overline{A}}^{\,2}}{N_{cal} (\sum_i \overline{A}_{i,cal}^{\,2}) - (\sum_i \overline{A}_{i,cal})^2} \tag{39}$$

$$\sigma_{\overline{A}}^{\,2} = \frac{1}{N_{cal} - 2} \sum_{i=1}^{N_{cal}} \left(X_{i,cal} - P_1 \overline{A}_{,cali} - P_2 \right)^2 \tag{40}$$

where $X_{i,cal}$ is the mole fraction of the calibration gas mixture at the ith point, $\overline{A}_{i,cal}$ is

the co-added absorbance at the ith point, and N_{cal} is the number of calibration points.

Note, however, that Equations 38-40 do not account for the fact that the values of

$X_{i,cal}$ and $\overline{A}_{i,cal}$ are themselves uncertain. The procedures for computing the

uncertainties in P_1 and P_2 while accounting for the uncertainties in $X_{i,cal}$ and $\overline{A}_{i,cal}$ are

much more involved and are discussed elsewhere [53-56]. The uncertainties are

estimated here using a FORTRAN subroutine 'fitexy' from [57] that implements the method described in [53-56].

A virtually identical procedure is used for determining the uncertainty in the CH_4 concentration measurements except that in one measurement method, the peak of the Q branch is used instead of the area under the vibrational band. Table 3 presents typical values for the various parameters of the uncertainty analysis discussed above.

Table 3: Typical values for the concentration uncertainty calculation

Concentration Calibration		Concentration CO_2		
δQ_{CO2}	δQ_{air}	δA	$\delta P1$	$\delta P2$
10	100	6.05E-05	2.44E-04	4.17E-05
SCCM	SCCM	cm^{-1}	moles/liter	moles/liter
Concentration CH_4			Both CO_2 and CH_4	
$\delta Peak$	$\delta P1$	$\delta P2$	RMS Noise	$\Delta \nu$
1.41E-04	9.21E-06	1.92E-04	7.20E-04	25
	moles/liter	moles/liter		cm-1

Uncertainty in Temperature

We begin by considering the residual from the temperature fitting procedure:

$$R = \sum_{i=1}^{N} A_{ex,i} - A_{fit,i} \qquad (41)$$

where $A_{ex,i}$ is the ith point of the experimentally measured absorbance spectrum, $A_{fit,i}$ is the ith point of the best fit to the absorbance spectrum, and N is the total number of points defining the spectrum. The measured and fitted absorbances can be written as follows:

$$A_{ex,i} = A_{real,i} \pm \sigma_{rms} \qquad (42)$$

$$A_{fit,i} = A_{perfect\ fit,i} \pm \left[\left. \frac{\partial f_i}{\partial T} \right|_C \delta T + \left. \frac{\partial f_i}{\partial C} \right|_T \delta C \right] \qquad (43)$$

where $A_{real,i}$ is the absorbance at point i in the absence of instrument errors and σ_{rms}

represents the instrument errors. $A_{perfect\ fi,i}$ is the absorbance at point i in the absence

of fitting, measurement *and* instrument errors while f is the EM2C function used to

compute the absorbance as a function of gas temperature and concentration. δC is

the uncertainty in the gas concentration which is known from the results of the

previous section and δT is the quantity we desire: the uncertainty in the temperature

measurement. Substitution of Equations 42 and 43 into 41 and incorporating the fact

that $A_{real,i} = A_{perfect\ fii,i}$ gives the following expression for the residual of the fit:

$$R = \sum_{i=1}^{N} \left\{ \pm \sigma_{rms} \mp \left[\left. \frac{\partial f_i}{\partial T} \right|_C \delta T + \left. \frac{\partial f_i}{\partial T} \right|_X \delta C \right] \right\} \qquad (44)$$

Note that even when the fit to the experimental data is perfect ($R=0$) and instrument

errors are zero, the uncertainty in the temperature still depends on the uncertainty in

the concentration measurement. Equation 44 can be re-written as follows:

$$R = \pm \alpha \mp \beta \delta T \qquad (45)$$

where α and β are constants that can be computed using σ_{rms}, f, and δC: and δT is a

multiplicative constant that can be moved out of the summation:

$$\alpha = \sum_{i=1}^{N} \left(\sigma_{rms} - \left. \frac{\partial f_i}{\partial C} \right|_T \delta C \right) \qquad (46)$$

$$\beta = \sum_{i=1}^{N} \left. \frac{\partial f_i}{\partial T} \right|_C \qquad (47)$$

Squaring both sides of Equation 45 gives the following expression that can be solved

for δT:

$$R^2 = \alpha^2 - 2\beta\delta T + \beta^2 (\delta T)^2 \tag{48}$$

It is worth noting that Equation 48 appears to have the proper behavior. When the fit to the experimental data is perfect ($R^2=0$), the uncertainty in the temperature will depend on the uncertainty in the instrument and the concentration measurement. When the uncertainty in the instrument is zero and the data fit is perfect, the uncertainty in the temperature depends only on the uncertainty in the concentration measurement. Only when the instrument, concentration measurement, and fit are all perfect, can the uncertainty in the temperature measurement be zero.

Solving Equation 49 for δT using the quadratic formula gives:

$$\delta T = \frac{2\beta \pm \sqrt{4\beta^2 - 4(\alpha^2 - R^2)\beta^2}}{2\beta^2} \tag{49}$$

There are two solutions to Equation 48 and the larger is taken as the uncertainty in the temperature. The asymptotic behavior of Equation 48 is also interesting. As $\alpha, R \to 0$, Equation 49 shows that $\delta T \to (0, 2/\beta)$. Since we choose the larger of the two solutions, the error does not necessarily go to zero as $\alpha, R \to 0$. In order to drive the uncertainty in temperature to zero in all cases, we need $\beta \to \infty$ or, we need to choose a spectral region with maximum sensitivity. Conversely, when the temperature sensitivity of the spectral region goes to zero, the uncertainty in temperature goes to infinity.

Appendix D – Matlab scripts calculating CO_2 and CH_4 concentration

CO2conc_full.m
```
% Script to open up all the files in a directory and calculate the concentration
clear all
close all

% Specify the directory
dir_name = 'C:\Work\CDEM Lab\Micro-Combustor\Data\May27';
curr_dir = pwd;


% Load files into memory
% open all the files and collect the z positions, wavelengths and absorbances
[z, nu_spectra, abs_spectra] = load_files(dir_name);

% Find rms noise in spectra
% Search in area of band with no interference from molecules
index(1) = Locate(nu_spectra,2500,20);
index(2) = Locate(nu_spectra,2700,20);

abs_rms = abs_spectra(index(1):index(2),:);

rms_noise = std(abs_rms);

% Locate area of interest, using binary search
ind(1) = Locate(nu_spectra,2000,20);
ind(2) = Locate(nu_spectra,2500,ind(1)+100);

% Define new variables based on band
nu_band = nu_spectra(ind(1):ind(2));
abs_band = abs_spectra(ind(1):ind(2),:);


% Do a baseline correction on the experimental data.
% Do a polynomial least squares fit using the end of the band 2050-2100 and 2450-
2550
[n,m] = size(nu_band);
ind(1) = Locate(nu_band,2100,5);
ind(2) = Locate(nu_band,2450,5);
[o,p] = size(z);
for i = 1:p
   % [P, S] = polyfit(nu(1:ind(1)),abs(1:ind(1)),1);
```

```matlab
    [P, S] =
polyfit([nu_band(1:ind(1));nu_band(ind(2):n)],[abs_band(1:ind(1),i);abs_band(ind(2
):n,i)],2);
    corr = P(1)*nu_band.^2 + P(2)*nu_band + P(3);
    abs_corr(:,i) = abs_band(:,i) - corr;
end

% Trim edges of region so we are calculating area under band
ind(3) = Locate(nu_band,2425,5);
nu_band = nu_band(ind(1):ind(3));
abs_corr = abs_corr(ind(1):ind(3),:);

% Calculate area
[n,m] = size(nu_band);
for i = 1:p
    area_exp(i) = sum(0.5*(abs_corr(1:n-1,i) + abs_corr(2:n,i)).*(nu_band(2:n)-
nu_band(1:n-1)));
end

% Open calibration files
conc_dir = 'C:\Work\CDEM Lab\Micro-Combustor\Data\calibration_CO2\May22';
cd(conc_dir);
load('CO2conc_cal.mat')
area_22 = area_band;
coeff_22 = area_coeff;
conc_22 = conc_mix;
error_conc_22 = error_conc;
cd(curr_dir)

% Open calibration files
conc_dir = 'C:\Work\CDEM Lab\Micro-Combustor\Data\calibration_CO2\May19';
cd(conc_dir);
load('CO2conc_cal.mat')
area_19 = area_band;
coeff_19 = area_coeff;
conc_19 = conc_mix;
error_conc_19 = error_conc;
cd(curr_dir)

area = [area_19,area_22];
conc = [conc_19,conc_22];
[area_coeff,s] = polyfit(area,conc,1);

% Find concentrations based on calibrated fits
conc_exp = area_coeff(1).*area_exp + area_coeff(2);
```

```matlab
% For area
sigma_area = sqrt(1/(length(area))*sum((conc -
(area_coeff(2)+area_coeff(1)*area)).^2));
delta = abs(length(area)*sum(area.^2) - sum(area)^2);
sigma_p1 = sqrt(sigma_area.^2*sum(area.^2)/delta);
sigma_p2 = sqrt(length(area)*sigma_area^2/delta);
error_conc = sqrt((area_exp*sigma_p1).^2 + sigma_p2.^2 +
(area_coeff(1)*sigma_area)^2);



% save results
cd(dir_name);
save('CO2conc_results.mat','z','conc_exp','area_exp','abs_corr','nu_band','error_conc')
cd(curr_dir);

error_area = 2*(2425-2100)*rms_noise;

save co2conc.txt conc_exp area_exp error_area error_conc -ASCII

% plot
figure
errorbar(z,conc_exp,error_conc,'*')
```

CH4conc_full.m
```matlab
% Script to open up all the files in a directory and calculate the concentration
clear all
close all

% Specify the directory
dir_name = 'C:\Work\CDEM Lab\Micro-Combustor\Data\17June04\run2';
curr_dir = pwd;


% Load files into memory
% open all the files and collect the z positions, wavelengths and absorbances
[z, nu_spectra, abs_spectra] = load_files(dir_name);

% Find rms noise in spectra
% Search in area of band with no interference from molecules
index(1) = Locate(nu_spectra,2500,20);
index(2) = Locate(nu_spectra,2700,20);

abs_rms = abs_spectra(index(1):index(2),:);

rms_noise = std(abs_rms);
```

```matlab
% Locate area of interest, using binary search
ind(1) = Locate(nu_spectra,2600,20);
ind(2) = Locate(nu_spectra,3400,ind(1)+100);

% Define new variables based on band
nu_band = nu_spectra(ind(1):ind(2));
abs_band = abs_spectra(ind(1):ind(2),:);

% Do a baseline correction on the experimental data.
% Do a polynomial least squares fit using the end of the band 2050-2100 and 2450-
2550
[n,m] = size(nu_band);
ind(1) = Locate(nu_band,2800,5);
ind(2) = Locate(nu_band,3250,5);
[o,p] = size(z);
for i = 1:p
   % [P, S] = polyfit(nu(1:ind(1)),abs(1:ind(1)),1);
   [P, S] =
polyfit([nu_band(1:ind(1));nu_band(ind(2):n)],[abs_band(1:ind(1),i);abs_band(ind(2
):n,i)],2);
   corr = P(1)*nu_band.^2 + P(2)*nu_band + P(3);
   abs_corr(:,i) = abs_band(:,i) - corr;
end

% Calculate max peak
[n,m] = size(nu_band);
for i = 1:p
   area_exp(i) = sum(0.5*(abs_corr(1:n-1,i)+abs_corr(2:n,i)).*(nu_band(2:n)-
nu_band(1:n-1)));
   peak_exp(i) = max(abs_corr(:,i));
end

% Open calibration files
conc_dir = 'C:\Work\CDEM Lab\Micro-Combustor\Data\calibration_CH4\May22';
cd(conc_dir);
load('CH4conc_cal.mat')
area_22 = area_band;
coeff_22 = area_coeff;
conc_22 = conc_mix;
error_conc_22 = error_conc;
max_peak_22 = max_peak;
cd(curr_dir)

% Open calibration files
conc_dir = 'C:\Work\CDEM Lab\Micro-Combustor\Data\calibration_CH4\May19';
```

```
cd(conc_dir);
load('CH4conc_cal.mat')
area_19 = area_band;
coeff_19 = area_coeff;
conc_19 = conc_mix;
error_conc_19 = error_conc;
max_peak_19 = max_peak;
cd(curr_dir)

area = [area_19,area_22];
max_peak = [max_peak_19,max_peak_22];
conc = [conc_19,conc_22];
[area_coeff,s] = polyfit(area,conc,1);
[peak_coeff,s] = polyfit(max_peak,conc,1);

% Find concentrations based on calibrated fits
conc_exp_area = area_coeff(1).*area_exp + area_coeff(2);
conc_exp_peak = peak_coeff(1).*peak_exp + peak_coeff(2);

% Find uncertainties of concentrations
% Calculate error
% Concentration for peaks
sigma_peak = sqrt(1/(length(max_peak))*sum((conc -
(peak_coeff(2)+peak_coeff(1)*max_peak)).^2));
delta = abs(length(max_peak)*(sum(max_peak.^2) - sum(max_peak)^2));
sigma_p1 = sqrt(sigma_peak.^2*sum(max_peak.^2)/delta);
sigma_p2 = sqrt(length(max_peak)*sigma_peak^2/delta);

error_conc_peak = sqrt((peak_exp*sigma_p1).^2 + sigma_p2.^2 +
(peak_coeff(1)*sigma_peak)^2);

% For area
sigma_area = sqrt(1/(length(area))*sum((conc -
(area_coeff(2)+area_coeff(1)*area)).^2));
delta_a = abs(length(area)*sum(area.^2) - sum(area)^2);
sigma_p1_a = sqrt(sigma_area.^2*sum(area.^2)/delta_a);
sigma_p2_a = sqrt(length(area)*sigma_area^2/delta_a);

error_conc_area = sqrt((area_exp*sigma_p1_a).^2 + sigma_p2_a.^2 +
(area_coeff(1)*sigma_area)^2);


% save results
cd(dir_name);
save('CH4conc_results.mat','z','conc_exp_area','conc_exp_peak','area_exp','abs_corr',
'nu_band','error_conc_peak','error_conc_area')
```

```
cd(curr_dir);

% plot
figure
plot(z,conc_exp_area,'*')
hold on
plot(z,conc_exp_peak,'ko')
errorbar(z,conc_exp_area,error_conc_area(1)*ones(length(z),1),'*')
errorbar(z,conc_exp_peak,error_conc_peak,'ko')
hold off
xlabel('Downstream distance from inlet (mm)')
ylabel('Concentration (moles/liter)')
legend('Area Method','Peak Method')
```

Bibliography

1.   Mikhaylik, Y.V. and J.R. Akridge, *300-400 Wh/kg Rechargable Li/S Batteries Operating at -60 to +65 degrees C.* IMLB 12 Meeting, Tucson AZ, 2004.

2.   Leach, T. and C. Cadou, *Effect of Structural Heat Conduction on the Power Density of Micro-Combustors.* AIAA, 2004.

3.   Glassman, I., *Combustion*. 3rd ed. 1996, Princeton: Academic Press.

4.   Buckley, S.G. and M.M. Ohadi, *High Temperature Heat Exchangers and Microscale Combustion Systems: Applications To Thermal System Miniaturization.* Experimental Thermal and Fluid Science, 2001. **25**: p. 207-217.

5.   Dellimore, K. and C. Cadou, *Fuel-Air Mixing Challenges In Micro-Power Systems.* AIAA-0301, 2004.

6.   Lewis and v. Elbe, *Combustion Flames and Explosions of Gases*. 1961, New York: Academic Press Inc.

7.   von Karman, T. and G. Millan, Proceedings of the Combustion Institute, 1953. **4**: p. 173-178.

8.   Friedman, R., Proceedings of the Combustion Institute, 1949. **3**: p. 110-117.

9.   Daou, J. and M. Matalon, *Influence of Conductive Heat-Losses on the Propagation of Premixed Flames in Channels.* Combustion and Flame, 2002. **128**: p. 321-329.

10.   Ronney, P.D., *Analysis of non-adiabatic heat-recirculating combustors.* Combustion and Flame, 2003. **125**: p. 421-439.

11. Cadou, C. and T. Leach, *The Role of Structural Heat Exchange and Heat Lose in the Design of Efficient Silicon Micro-combustors.* 30th International Symposium on Combustion, 2004.

12. Raimondeau, S., D.A. Norton, D.G. Vlachos, and R.I. Masel, *Modeling of high temperature microburners.* Proceedings of the Combustion Institute, 2003. **29**: p. 901-907.

13. Fernandez-Pello, A., *Micropower Generation Using Combustion: Issues and Approaches.* Proceedings of the Combustion Institute, 2002. **29**: p. 883-899.

14. Mehra, A., X. Zhang, A.A. Ayon, I.A. Waitz, M.A. Schmidt, and C.M. Spadaccini, *A Six-Wafer Combustion System for a Silicon Micro Gas Turbine Engine.* Journal of MicroElectroMechanical Systems, 2000. **9**(4): p. 517-527.

15. Aichlmayr, H.T., D.B. Kittelson, and M.R. Zachariah, *Miniature free-piston homogeneous charge compression ignition engine-compressor concept- Part I: performance estimation and design considerations unique to small dimensions.* Chemical Engineering Science, 2002. **57**(4161-4171).

16. Aichlmayr, H.T., D.B. Kittelson, and M.R. Zachariah, *Micro-HCCI combustion: experimental characterization and development of a detailed chemical kinetic model with coupled piston motion.* Combustion and Flame, 2003. **135**: p. 227-248.

17. Kirtas, M., M. Disseau, D. Scarborough, J. Jagoda, and S. Menon, *Combustion Dynamics in a High Aspect Ratio Engine.* Proceedings of the Combustion Institute, 2002. **29**: p. 917-923.

18.   Ronney, P.D., K. Takeda, K. Maruta, L. Sitzki, and K. Borer, *Catalytic Combustion in Microchannel for MEMS Power Generation.* The Third Asia-Pacific Conference on Combustion, 2001.

19.   Ronney, P.D., F.J. Weinberg, D.M. Rowe, and G. Min, *On Thermoelectric Power Conversion from Heat Recirculating Combustion Systems.* Proceedings of the Combustion Institute, 2002. **29**: p. 941-947.

20.   Yetter, R.A., J. Vican, B.F. Gajdeczko, F.L. Dryer, D.L. Milius, and I.A. Aksay, *Development of a Microreactor as a Thermal Source for Microelectromechanical Systems Power Generation.* Proceedings of the Combustion Institute, 2002. **29**: p. 909-916.

21.   Zhang, X., A. Mehra, A.A. Ayon, and I.A. Waitz, *Igniters and temperature sensors for a micro-scale combustion system.* Sensor and Actuators, 2003. **103**: p. 253-262.

22.   Epstein, A.H., S.D. Senturia, and U. Al-Midani, *Micro-Heat Engines, Gas Turbines and Rocket Engines - The MIT Microengine Project.* Twenty-Eigth AIAA Fluid Dynamics Conference 97-1773, 1997.

23.   Breuer, K., G. Han, J.C. Bird, J.A. Westin, and Z. Cao, *Infrared Diagnostics For Measuring Fluid and Solid Motion Inside Silicon Microdevices.* Microscale Thermophysical Engineering. **8**(2): p. 169-182.

24.   Jacquot, O. and P. Herve, *Determination of temperature fields in exhaust gases by infrared spectroscopy.* Proceedings of SPIE, 1998. **3493**: p. 71-78.

25.   Heland, J., K. Schafer, and R. Haus, *Investigations of Hot Exhaust Gases with Passive FTIR Emission Spectroscopy.* Proceedings of SPIE, 1998. **3493**: p. 2-10.

26.   Hilton, M., A.H. Lettington, and I.M. Mills, *Quantitative Analysis of Remote Gas Temperatures and Concentrations from Their Infrared Emmission Spectra.* Measurement Science and Technology, 1995. **6**: p. 1236-1241.

27.   Bailly, D., C. Camy-Peyret, and R. Lanquetin, *Temperature Measurements in Flames through CO2 and CO Emission: New Highly Excited Levels of CO2.* Journal of Molecular Spectroscopy, 1997. **182**: p. 10-17.

28.   Lindner, J.S., Z. Hansheng, and R.L. Cook, *Non-intrusive Determination of Combustion Efficiency Using FTIR Spectroscopy.* Proceedings of SPIE, 1995. **2365**: p. 285-301.

29.   Koshland, C.P., D. Lucas, B.S. Higgins, and R.F. Sawyer, *Detection of Chlorinated Hydrocarbons in Combustion Using In-Situ FTIR Spectroscopy.* Twenty Fourth Symposium (International) on Combustion, 1992: p. 1597-1604.

30.   Modest, M. and S.P. Bharadwaj, *Medium Resolution Transmission Measurements of CO2 at High Temperature.* Journal of Quantitative Spectroscopy and Radiative Transfer, 2002. **73**: p. 329-338.

31.   Hara, H. and Y. Nishi, J. Phys. Soc. Jpn, 1966. **21**(6): p. 1222.

32.   Spitzer, W. and H.Y. Fan, Physics Review, 1957. **108**(2): p. 268-271.

33.   Herzberg, G., *Molecular Spectra and Molecular Structure, Vol. I, Spectra of Diatomic Molecules*. 7 ed. 1950, Princeton: D. Van Nostrand Co. Inc.

34. Rothman, L.S., *AFGL atmospheric absorption line parameters compilation: 1980 version.* Applied Optics, 1981. **20**: p. 791.

35. Gharavi, M. and S.G. Buckley, *Diode Laser Absorption Spectroscopy Measurement of Line Strengths and Pressure Broadening Coefficients of the Methane 2v3 Band at Elevated Temperatures.* 3rd Joint Meeting of the U.S. Sections of the Combustion Institute. Chicago, Il, 2003.

36. Rothman, L.S. and et al., *The HITRAN Molecular Spectroscopic Database and HAWKS (HITRAN Atmospheric Workstation): 1996 Edition.* 1996.

37. Rothman, L.S., *The HITRAN molecular spectroscopic database: edition 2000 including updates through 2001.* Journal of Quantitative Spectroscopy and Radiative Transfer, 2003. **82**: p. 5-44.

38. Anderson, G.P., F.X. Kneizys, and L.S. Rothman, *FASCODE/MODTRAN/LOWTRAN: Past/Present/Future.* 1994.

39. Smith, H.J.P., D.J. Dube, M.E. Gardner, S.A. Clough, F.X. Kneizys, and L.S. Rothman, *FASCODE - Fast Atmospheric Signature Code (Spectral Transmittance and Radiance).* AFGL-TR-78-0081, 1978.

40. Grosshandler, W., *RADCAL: A Narrow-Band Model for Radiation Calculations in Combustion Enviroment.* NIST Technical Note 1402, 1993.

41. Soufani, A. and J. Taine, *High temperature gas radiative property parameters of statistical narrow-band model for H2O, CO2 and CO and correlated K-model for H2O.* International Journal of Heat Transfer, 1997. **40**(4): p. 987-991.

42. Malkmus, W., *Random band Lorentz with exponential tailed 1/S line-intensity distribution function.* Journal of the Optical Society of America, 1967. **57**: p. 323-329.

43. Young, S.J., *Nonisothermal band model theory.* Journal of Quantitative Spectroscopy and Radiative Transfer, 1978. **18**: p. 1-28.

44. Runyan, W.R., *Technology Semiconductor Silicon*. 1966: McGraw-Hill Book Company.

45. Born, M. and E. Wolf, *Principles of Optics Electromagnetic Theory of Propogation Interference and Diffraction of Light*. 6 ed. 1980, New York: Pergamon Press.

46. Shaddix, C., *Practical Aspects of Correcting Thermocouple Measurements for Radiation Loss.* Western States Meeting of the Combustion Institute, Fall 1998.

47. Incropera, F.P. and D.P. DeWitt, *Fundamentals of Heat and Mass Transfer*. 5 ed. 2002, New York: John Wiley and Sons.

48. Kays, W.M. and M.E. Crawford, *Convective Heat and Mass Transfer*. 1993, New York: McGraw-Hill Inc.

49. Mills, A.F., *Basic Heat and Mass Transfer*. 1995, Chicago: Irwin.

50. http://www.c.morley.ukgateway.net/gseqmain.htm.

51. Taylor, J., *Introduction to Error Analysis*. 2nd ed. 1997: University Science Books.

52. *Test Uncertainty.* AMSME PTC, 1998. **19.1**.

53. Reed, B.C., American Journal of Physics, 1989. **57**: p. 642-646.

54. Reed, B.C., American Journal of Physics, 1990. **58**: p. 189.

55. Reed, B.C., American Journal of Physics, 1990. **58**: p. 1209.

56. Reed, B.C., American Journal of Physics, 1992. **60**: p. 59-62.

57. Press, W.H., S.A. Teukolsky, W.T. Vetterling, and B.P. Flannery, *Numerical Recipes in FORTRAN*. 1992, Cambridge.